High performance photon-pair source based on a fiber-coupled periodically poled $KTiOPO_4$ waveguide

by

Tian Zhong

Submitted to the Electrical Engineering and Computer Science
in partial fulfillment of the requirements for the degree of

Master of Science

at the

MASSACHUSETTS INSTITUTE OF TECHNOLOGY

June 2009

Author .....
.....
Electrical Engineering and Computer Science
May 22, 2009

Certified by....
....
Franco N. C. Wong
Senior Research Scientist
Thesis Supervisor

Accepted by.....
.....
Terry P. Orlando
Chairman, Departmental Committee on Graduate Students

High performance photon-pair source based on a fiber-coupled periodically poled $KTiOPO_4$ waveguide

by

Tian Zhong

Submitted to the Electrical Engineering and Computer Science
on May 22, 2009, in partial fulfillment of the
requirements for the degree of
Master of Science

Abstract

Photon-pair sources based on spontaneous parametric downconversion (SPDC) in a nonlinear crystal waveguide have been shown to be significantly more efficient than those in a bulk crystal. To utilize waveguide sources in quantum information processing (QIP) applications, it is highly desirable to integrate additional functionality such as pump sources and modulators at the waveguide-chip level for compactness, reliability, and ease of operation. As a first step we develop a waveguide SPDC source with integrated single-mode polarization-maintaining (PM) fibers in this thesis work, and demonstrate the efficient generation of photon pairs at 1316 nm in a type-II phase-matched Rb-indiffused waveguide in periodically poled $KTiOPO_4$ (PPKTP). We perform the flux and spectrum characterization of our integrated waveguide source, and obtain a pair production rate of 2×10^7/s/mW in a 1.08-nm bandwidth. The measurement results are in good agreement with a theoretical model that takes into account the transversal momentum imparted on the phase matching function by the waveguide. With narrowband filtering and a pump power, we achieve a Hong-Ou-Mandel quantum-interference visibility of 98.2% after subtraction of accidental coincidences, representing the highest reported value for a waveguide-based photon-pair source. The photon-pairs generated by our PPKTP waveguide are shown to be highly indistinguishable, in terms their spectra and spatial modes. Therefore the fiber-coupled waveguide source is particularly suitable for long-distance quantum communication protocols such as fiber-based quantum key distribution (QKD).

Thesis Supervisor: Franco N. C. Wong
Title: Senior Research Scientist

Acknowledgments

I am grateful to my advisor, Dr. Franco N.C. Wong, for his mentorship and advising. His expertise in experimental optics and enormous patience helped me transit into this field from my previous background. I came with zero experience in nonlinear optics and quantum information science, but Dr. Wong has always been open to my questions, and has guided me through even the most tiny experimental details. Without his support and encouragement this thesis would not have been done. I would also like to thank Prof. Jeffrey H. Shapiro for his excellent teaching and theoretical insight. His superb lectures on quantum optical communications were not only inspirational but also extremely helpful for understanding the theoretical underpinnings of our work. Furthermore, I feel privileged to know the former graduate students at RLEs Optical and Quantum Communications Group. I am thankful to Dr. Taehyun Kim for his openness and a sense of responsibility for every question I raised to him. We had a good time working in the same office. I also thank Dr. Onur Kuzucu for his help on my experiments. I always enjoyed our discussions on lab work and I truly appreciate his generosity.

I thank Tony D. Roberts and Philip Battle from AdvR for the fiber-coupled waveguide fabrication, for their advices on operating the device, and for their insightful review for our papers.

The rest of my thanks goes to my wife. Her presence in Cambridge has always been a comfort for me. And I thank her for the emotional support throughout my study.

This work was supported in part by the Intelligence Advanced Research Projects Activity (IARPA) through NIST Grant 70NANB7H6186 and by the Department of Interior Contract NBCHC060071.

Contents

List of Figures

List of Tables

Chapter 1

Introduction

The development of quantum mechanics has opened up new opportunities in many well-established fields such as communication theory, coding and error correction, cryptography, and metrology. Using the idea of entanglement many schemes have been proposed for providing secure communication between two parties [1, 2], realizing polynomial-time computation for classically intractable problems [3, 4], and beating the standard quantum limit in precision metrology [5, 6]. The essence of these new schemes lies in the superposition of quantum states, which can be experimentally realized by encoding onto the physical properties of a quantum object, such as an atom, an ion, or a photon. Among all the physical systems that can implement quantum information processing (QIP) tasks, photon is an unbeatable choice for long-distance transmission of quantum information. Because of its limited interaction with the environment and other photons, a photonic quantum system suffers minimal decoherence. Up to date, photonic entanglement has been demonstrated in many degrees of freedom, such as polarization, momentum, frequency, time-bin, etc. It has been extensively used for testing the validity of quantum mechanics, superdense encoding of classical information [7, 8] , and the security limits of today's quantum key distribution (QKD) technology [2, 9, 10].

Various QIP applications require task-specific engineering of the quantum state of single photons or pairs of photons. In this work, we exclusively use spontaneous parametric downconversion (SPDC) for the generation, modification and character-

ization of photon pairs. SPDC is a nonlinear three-wave mixing process in which a single energetic pump photon is converted into a pair of photons called signal and idler that obey energy and momentum conservation. Over the years, SPDC has been established as an efficient technique that can be characterized in various degrees of freedom such as polarization, frequency, momentum and orbital angular momentum. As compared to other single- or few-photon emitters, such as quantum dots [11] or four-wave mixing in fibers [12, 13, 14], SPDC shows a flexible control over the relevant degrees of freedom, which is desirable for photonic quantum-state engineering. For the above reasons, SPDC has been extensively used in many QIP applications such as QKD [15, 16, 17], quantum teleportation [18] and cluster-state quantum computation [19, 20, 21]. SPDC has also been utilized for generating two-photon states that are entangled in multiple degrees of freedom [7, 8, 9].

SPDC is typically implemented using a nonlinear bulk crystal. Depending on the focusing of the pump beam, a bulk crystal SPDC source generally produces a complicated emission pattern. A typical output has a distribution of a cone shape, which consists of multiple spatial modes of the signal and idler fields. To obtain a high quantum interference visibility, it is necessary to use an iris to collect only a few spatial modes from the entire emission pattern. Consequently, the usable photon-pair flux is low for a bulk SPDC process. Moreover, the complicated output pattern makes it very difficult to couple the photon-pair flux into a single mode fiber for long-distance transmission. One solution to this problem is to use a nonlinear waveguide for SPDC photon-pair production. The idea is that the mode confinement provided by the waveguide could lead to a true single spatial mode emission at the output, thus allowing all of the SPDC output be easily coupled into a single mode fiber.

Photon-pair sources based on SPDC in a nonlinear crystal waveguide have been shown to be significantly more efficient than those in a bulk crystal [22, 23, 24, 25, 26, 27]. To utilize waveguide sources in QIP applications, it is highly desirable to integrate additional functionality such as pump sources and modulators at the waveguide-chip level for compactness, reliability, and ease of operation. As a first step we are interested in developing a waveguide SPDC source with integrated single-mode

polarization-maintaining (PM) fibers. The designed output are frequency-degenerate, orthogonal signal and idler photon-pairs at the telecom wavelength of 1316 nm. The waveguide was fabricated by AdvR on a periodically poled $KTiOPO_4$ (PPKTP) nonlinear crystal with type-II phase-matching. The choice of KTP as the nonlinear material takes advantage of its large temperature tuning bandwidth, so the device can withstand relatively large temperature fluctuations while still maintaining a highly degenerate output with excellent stability. The fiber-coupled waveguide source is particularly suitable for long-distance quantum communication protocols such as fiber-based QKD [29, 30, 31]. By connecting the source to a standard single mode fiber, we can easily distribute the photon pairs at telecom band with minimum attenuation. The operating wavelength of 1316 nm allows the QKD network to coexist with the standard 1.55 μm telecommunication fiber-optic infrastructure with minimal effects due to cross-talk and nonlinear spurious signals. Additionally, the generated photons automatically share the same spatial mode in the fiber. With a complete erasure of spatial mode distinguishability, the photon pairs can be utilized to demonstrate high visibility quantum interference and entanglement.

Two key performance metrics for a photon-pair source are the spectral brightness and the degree of indistinguishability for the photon pairs. Source spectral brightness of a nonlinear crystal waveguide in units of generated pairs/s per mW of pump power per nanometer of bandwidth has been shown to greatly exceed that of its bulk crystal counterpart. Reference [26] reported a 50-fold enhancement in the generation rate of a PPKTP waveguide over that of a bulk PPKTP crystal and attributed it to a much larger density of states for the waveguide. We investigate the origin of this significant increase in the density of states using a different theoretical model of waveguide SPDC generation. We modify the standard phase matching function of a nonlinear medium by including the transverse wave vector imposed by the cross-sectional index profile of the waveguide and arrive at the same analytical result as that found in Ref. [26]. Our model, therefore, gives a simple physical picture of the waveguide generation rate and may lead to improved design of waveguide sources.

An important usage of a photon-pair source is the generation of entangled pho-

tons. For example, one can separate orthogonally polarized frequency-degenerate signal and idler photon pairs and use a 50-50 non-polarizing beam splitter to generate polarization-entangled photons postselectively [32]. The entanglement quality of such a SPDC source can be estimated by how indistinguishable the signal and idler photons are, as measured by their Hong-Ou-Mandel (HOM) quantum interference [33]. Previous HOM measurements of waveguide sources have not shown a high quantum-interference visibility and high-quality polarization entanglement has not been obtained from these waveguide sources. In this work, we have measured a HOM visibility of 98.2% after subtraction of accidental coincidences caused mostly by the high dark count rates of InGaAs single-photon detectors. The high HOM visibility of our waveguide device suggests that it is a suitable source for many QIP applications that require compactness, high spectral brightness, and a high degree of indistinguishability.

1.1 Comparison of Waveguide SPDC Sources

Waveguide SPDC sources at different wavelengths have been realized recently [26, 24, 27, 28]. Their performances are summarized in Table 1.1, from which we can identify the remaining challenges in making waveguide source outperform its bulk crystal counterpart. For comparison, we also include in the list a state-of-art bulk PPKTP SPDC source [26, 32]. We find that even with an open iris to collect all spatial modes, the total flux produced by a bulk source is significantly lower than a waveguide source. Except for the pulsed PPKTP source [24], cw pumped waveguides generally have pair production rates on the order of 10^7 pairs/s/nm/mW. The type-II phase-matched periodically poled lithium niobate (PPLN) waveguide in Ref. [28] has a significantly longer length of 3 cm, so its flux is correspondingly higher. For PPKTP material, we see clearly a high level of fluorescence photons in the output flux for waveguide sources, which is 5 times more than that observed in the bulk crystal case. Such a phenomenon is not well understood, but a large amount of fluorescence is certainly undesirable because it reduces the signal-to-noise ratio of any measurement

taken on the generated photon pairs. Furthermore, all the current waveguide sources seem to suffer from a poor HOM visibility. The best value reported is 79% from [26], which is still far worse than that of a bulk PPKTP source. Note that some references used different definitions of HOM visibility, and the numbers given in Table 1.1 are converted from the original results to be in line with our standard definition shown in chapter 5.

Comparison of Waveguide SPDC Sources				
Source material type-II phase-matched	λ_{spdc} (nm)	Brightness (pairs/s/nm/mW)	Fluorescence P_{fl}/P_{spdc}	HOM visibility
PPKTP(cw)[26]	810	7.3×10^7	~25%	79%
PPKTP(pulse)[24]	805	$\sim2.9\times10^6$	~38%	unknown
PPLN(cw)[27]	1310	3.7×10^7	unknown	74%
PPLN(cw)[28]	1554	9.2×10^7	unknown	54%
PPKTP bulk (cw)	795	1.5×10^6[26]	~5%	97.7%[32]

Table 1.1: List of waveguide SPDC sources and their key performances. We also include a state-of-art bulk PPKTP source as a baseline for comparison. Note that the brightness are normalized values in unit of generated pairs/s/nm/mW, and the HOM visibilities are converted from the originally reported data to be in line with the standard visibility definition given in chapter 5. For the bulk source, the brightness was measured with the iris open, so as to include the total flux of all spatial modes. The HOM visibility was measured with a small iris, so that only flux from a small number of modes was collected. PPKTP: periodically poled $KTiOPO_4$; PPLN: periodically poled lithium niobate.

To fully exploit the advantages of waveguide SPDC generation, we need to overcome the challenge of high fluorescence background and poor HOM visibility. In this work, we attempt to lower the fluorescence noise by pumping the waveguide at a longer wavelength and using a single mode fiber as a spatial filter to block unwanted fluorescence photons. The pump-induced fluorescence is expected to be multi-mode in nature, thus only a small fraction of them falls into a specific waveguide propagating mode, which then can be coupled into an output fiber. To obtain a high HOM visibility, we focus on careful engineering of the signal and idler spectra. We propose to use narrowband filtering to ensure a high degree of spectral overlap between the

signal and idler photons. Moreover, we set up the HOM experiment with a fiber 50-50 beam splitter, so all the photons are forced to be in the same spatial mode. When perfect indistinguishability is achieved on the two-photon state, the only factor that can degrade HOM measurement is the multi-pair generation. Therefore, we should pump the source with a power low enough that the probability of multi-pair generation events is negligibly small. With the above efforts, the PPKTP waveguide in this work measured an amount of fluorescence of 2% of the downconverted photons over the phase-matching bandwidth of 1.1 nm. Also, we achieve a HOM interference visibility of 98.2% after subtraction of accidental coincidences, representing the highest reported value for a waveguide-based photon-pair source.

1.2 Thesis Organization

This thesis is organized as follows. We first present our theory of waveguide SPDC generation in chapter 2. This alternative theoretical model is developed based on a modified phase matching function that takes into account of the waveguide's transverse index profile and imposed transverse momentum. We show that our theory gives a signal power density expression that is identical to the density of states formalism. While the density of states theory attribute the enhanced waveguide SPDC flux to a much larger density of the excitation modes, we suggest that it is a result of the enlarged effective angular divergence in waveguide SPDC. In chapter 3, we move on to the details of the fabrication and packaging of the fiber-coupled PPKTP waveguide source. The waveguide was fabricated by ion diffusion using at AdvR inc. We perform extensive simulations on the spatial mode profiles of the relevant interacting fields. Besides the fundamental mode process, we discuss the possibility of higher-order mode waveguide SPDC, and their potential effects on the output flux measurement. Next, we present our flux and spectrum characterization in chapter 4. First, we estimate the KTP nonlinear coefficient and the phase matching condition of the waveguide using second harmonics generation. Second, coincidence counting experiment between the signal and idler photons is shown. We compare the measured

SPDC flux to the theoretical predication at various pump powers. Third, by using a narrowband filter, we measure the spectral histogram of single photons, revealing the SPDC spectral bandwidth as well as the amount of fluorescence photons in the output flux. In chapter 5, we show the HOM quantum interference measurements on our waveguide source. We demonstrate a high HOM interference visibility by using a narrowband filter to eliminate any spectral distinguishability between the two photons. We discuss the effect of multi-pair generations as a limiting factor on the experimental HOM visibility, and we derive a fundamental relationship between the visibility and the mean pair generation rate. At the end of chapter 5, we also present the result of HOM interference without narrowband filtering, from which we accurately obtain the two-photon phase matching bandwidth. Finally, chapter 6 concludes the thesis with a summary of contributions and future prospects of the presented work for quantum information processing.

Chapter 2

Theory of Waveguide SPDC

2.1 Introduction

SPDC generation efficiency in bulk crystals is typically in the range of 10^{-12} to 10^{-8}, depending on the type of crystal, the crystal length, collection angle and bandwidth. Moreover, the total output flux from a bulk crystal is linearly proportional to the pump power and is not dependent on pump focusing. On the other hand, several groups have demonstrated that a nonlinear waveguide yields a significantly higher SPDC efficiency [22, 23, 24, 26, 27, 34]. Fiorentino *et al.* made a direct comparison between the outputs from a waveguide on PPKTP and a bulk PPKTP crystal. A 50-fold enhancement was observed in the case of the waveguide, and the result was in agreement with a semiclassical model based on the density of states of guided mode fields [26]. The model suggests that the waveguide supports a much larger density of states than its bulk crystal counterpart. According to this model, the electric field operators for the quantized signal and idler fields are

$$\hat{E}_{s,i} = \frac{i}{2}\sum_{k}[(\frac{2\hbar\omega_{s,i}}{n_{s,i}^2\epsilon_0})^{1/2}\frac{1}{\sqrt{L}}U_{s,i}^{(k)}(x,y)e^{i(\beta_{s,i}z-\omega_{s,i}t)}\hat{a}_{s,i} + h.c.] \tag{2.1}$$

where $\omega_{s,i}$ is the angular frequency, $n_{s,i}$ is the effective mode index, $\beta_{s,i}$ is the propagation constant, L is the length of the waveguide, and $\hat{a}_{s,i}$ is the annihilation operator for the signal (idler) field. $U_{s,i}^{(k)}(x,y)$ is the k^{th} transverse mode profile, satisfying the

normalization condition $\int_A \mathrm{d}x\mathrm{d}y|U^{(k)}| = 1$. The summation is over all the waveguide modes k, and $h.c.$ denotes the Hermitian conjugate. Similarly, the classical pump field can be written as

$$E_p = \frac{1}{2}[(\frac{2P_p}{cn_p\epsilon_0})^{1/2}U_p(x,y)e^{\imath(\beta_p z-\omega_p t)} + c.c.] \tag{2.2}$$

where P_p is the pump power, n_p is the pump mode index, ω_p is the pump angular frequency, $U_p(x,y)$ is the pump transverse mode profile, and $c.c.$ denotes the complex conjugate. The three-wave mixing process between a classical pump field and two quantized signal and idler fields can be studied in the interaction picture. In this approach, the joint state of the downconverted photons is perturbatively calculated by introducing an interaction Hamiltonian $\hat{H}_{int}$ defined over the effective interaction volume V.

$$\hat{H}_{int} = -\frac{\epsilon_0 d_{eff}}{2}\int_V \mathrm{d}^3\mathbf{r}E_p\hat{E}_s^+\hat{E}_\imath^+ + h.c. \tag{2.3}$$

where $\hat{E}_{s,\imath}^+$ is the positive frequency component of Eq. (2.1), and d_{eff} is the effective nonlinear coefficient. Note that among many possible combinations of the frequency components of $E_p, E_s, E_\imath$, we only keep the terms containing $e^{(\omega_p-\omega_s-\omega_\imath)t}$, because only those terms satisfy the energy conservation $\omega_s+\omega_\imath = \omega_p$. The interaction Hamiltonian in Eq. (2.3) allows the calculation of downconversion rate through Fermi's Golden rule, provided that one knows the density of states of the final output. This model treats the waveguide SPDC as a 1-dimensional problem. In a length scale of L, the 1-D density of states for either signal or idler field is,

$$\rho_{s,\imath} = \frac{Ln_{s,\imath}}{2\pi\hbar c} \tag{2.4}$$

The density of states for the two-photon output is then the convolution of the individual density of states for signal and idler fields, with the energy conservation condition $\mathrm{d}E_s = -\mathrm{d}E_\imath$,

$$\rho = (\frac{L}{2\pi})^2\frac{n_s n_\imath}{\hbar c^2}\mathrm{d}\omega_s \tag{2.5}$$

Using Eq. (2.1-2.5), the downconversion rate γ, or equivalently the downconverted signal power $\mathrm{d}P_s = \hbar\omega_s\gamma$ within a bandwidth $\mathrm{d}\lambda_s$ can be calculated to be [26]

$$\mathrm{d}P_s = \frac{16\pi^3\hbar d_{\mathrm{eff}}^2 L^2 c P_p}{\epsilon_0 n_s n_i n_p \lambda_s^4 \lambda_i} \frac{1}{A_I} \mathrm{sinc}^2\left(\frac{\Delta k_z L}{2}\right) \mathrm{d}\lambda_s\,, \tag{2.6}$$

where n_k is the waveguide mode index at wavelength λ_k for subscript k being signal s, idler i, or pump p, and A_I is the mode overlap area of the three interacting fields, defined as following:

$$A_I = \left(\int_A \mathrm{d}x\mathrm{d}y U_p U_s^* U_i^*\right)^{-2}, \tag{2.7}$$

For type-II first-order quasi-phase matching in PPKTP with a grating period Λ, the effective second-order nonlinear coefficient is $d_{\mathrm{eff}} = (2/\pi)d_{24}$ and the momentum mismatch is

$$\Delta k_z = \beta_p - \beta_s - \beta_i - \frac{2\pi}{\Lambda} \tag{2.8}$$

where β_j is the propagation constant in the waveguide along the propagation axis z.

This semi-classical approach for waveguide SPDC can be compared with the one used for bulk crystals in [36]. The main difference is that in a waveguide only three modes effectively interact, whereas in a bulk crystal case, the pump gaussian mode interacts with a continuum of plane-wave modes. The waveguide emission is confined to a limited band due to the sinc-squared function, whereas the bulk SPDC emission theory predicts that far from collinear emission the spectral density is almost flat, as experimentally verified in [37]. Based on the density of states model, this spectral difference is due to the fact that waveguide SPDC is essentially a 1 dimensional problem while the bulk has to be treated as a 3 dimensional case, because one has to consider the interaction of the pump with all plane waves. The resulting effect is not dissimilar from the spectral redistribution observed in SPDC experiments inside cavities [38]. Regarding a much brighter waveguide SPDC emission as compared to the bulk, the model suggests that a waveguide has the ability to increase mode overlap between the pump, signal, and idler, therefore, the interaction between the three fields can be enhanced. Additionally, from Eq. (2.6), we clearly see the spectral

density in a waveguide depends on L^2 whereas in bulk it depends on L. However, in the former case, as the crystal length increases, the width of the spectrum decreases. So the power integrated over the whole emission spectrum still grows linearly with L for waveguide SPDC.

Perhaps the most significant finding in Eq. (2.6) is that the waveguide SPDC spectral brightness is inversely proportional to the mode overlap area A_I, and therefore field confinement could lead to an enhanced pair generation rate. It is suggested that the output flux is higher due to the larger density of states (excitation modes) in a waveguide [26]. However, it is not obvious how to relate the density-of-states model for a waveguide to the standard model of SPDC in a bulk crystal that has no dependence on the pump beam area [35, 36]. This apparent contradiction on the area dependence of SPDC efficiency motivates us to seek for a more fundamental and intuitive understanding of the physical origin of the enhanced waveguide SPDC efficiency. In this chapter, we develop an alternative theoretical model of waveguide SPDC that incorporates a natural extension of the conventional phase-matching function by taking into account the transverse momentum imposed by the waveguide. The new theory can be verified by comparing it with the density of states formalism as well as the experimental results. Lastly, our transverse momentum theory should provide an estimate for the pair production rate of our fiber-coupled PPKTP waveguide source.

2.2 Transverse Momentum Theory

In a bulk crystal with a propagation geometry shown in Fig. 2-1 the SPDC signal output power within a $\mathrm{d}\lambda_s$ bandwidth is [39]

$$\mathrm{d}P_s = \frac{16\pi^3\hbar d_{\mathrm{eff}}^2 L^2 c P_p}{\epsilon_0 n_s n_i n_p \lambda_s^4 \lambda_i} \int \frac{1}{2\pi} k_s^2 \phi_s f(\lambda_s, \phi_s) \mathrm{d}\phi_s \mathrm{d}\lambda_s \,, \tag{2.9}$$

where ϕ_s is the angle between the signal wave vector $\vec{k}_s$ and pump wave vector $\vec{k}_p$. Most of the signal output comes from a narrow signal cone, beyond which the phase-matching function $f(\lambda_s, \phi_s) = \mathrm{sinc}^2(\Delta k_z L/2)$ is negligibly small to contribute. Con-

sider the momentum mismatch for the longitudinal (z) component,

$$\Delta k_z = k_{pz} - k_{sz} - k_{\imath z} - \frac{2\pi}{\Lambda}\,, \tag{2.10}$$

where k_{jz} is the wave vector $\vec{k}_j$ in the material projected along the propagation axis z, and for the transverse component

$$\Delta k_t = -k_{st} - k_{\imath t}\,, \tag{2.11}$$

where, without loss of generality, we assume that the pump propagates along the z principal axis so that there is no walk-off due to double refraction and that $k_{pz} = k_p$. For signal and idler propagating at small angles relative to the pump, $\phi_s, \phi_\imath \ll 1$, the z-component of the signal and idler wave vectors can be expressed in terms of their transverse wave numbers k_{jt} to second order:

$$k_{jz} = k_j - \frac{k_{jt}^2}{2k_j}\,, \qquad j = s, i \tag{2.12}$$

and the longitudinal momentum mismatch Eq. (2.10) becomes

$$\Delta k_z = \left(k_p - k_s - k_\imath - \frac{2\pi}{\Lambda}\right) + \frac{1}{2}\left(\frac{k_{st}^2}{k_s} + \frac{k_{it}^2}{k_\imath}\right)\,. \tag{2.13}$$

The first term on the right of Eq. (2.13) is the standard phase-matching condition for collinear propagation, whereas the second term is the additional contribution from the transverse signal and idler components for noncollinear propagation.

The transverse momentum matching of Eq. (2.11) dictates that the signal and idler transverse components are equal and opposite, $k_{st} = -k_{\imath t}$. For the case of frequency-degenerate SPDC in type-II phase-matched PPKTP, $\lambda_s = \lambda_\imath$ and $n_s \approx n_\imath$, and therefore $k_s \approx k_\imath$ and $\phi_s \approx -\phi_\imath$. The standard phase matching condition for collinear propagation is $\Delta k_z = 0$ with $k_{st} = -k_{\imath t}$ so that Eq. (2.13) is simplified to

$$\Delta k_z \approx \frac{k_{st}^2}{k_s}\,. \tag{2.14}$$

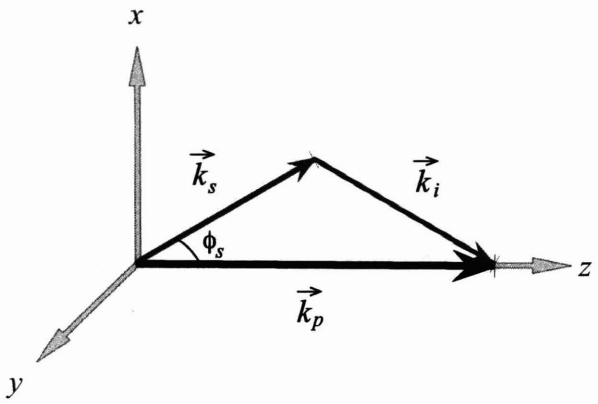

Figure 2-1: Geometry of noncollinear propagation of pump $\vec{k}_p$, signal $\vec{k}_s$, and idler $\vec{k}_i$.

From the phase-matching function $f(\lambda_s, \phi_s)$, we can obtain the phase-matching angular bandwidth by setting $\Delta k_z L = \pi$ which yields a divergence angle for SPDC in a bulk crystal of

$$\phi_{bulk}^{\text{div}} = \sqrt{\frac{\pi}{Lk_s}}, \tag{2.15}$$

Now let us consider an ideal rectangular waveguide with dimensions $w_x \times w_y$ and a uniform index Δn higher than the surrounding nonlinear material. The transverse index profile of the material, including both the waveguide and its surrounding, is a boxcar function with width w_x (w_y) along the x (y) dimension. The 2D index profile induces a transverse momentum vector $\vec{k}_{gt}$ that must be included in the transversal momentum mismatch of Eq. (2.11). Similar to the longitudinal grating momentum added by periodic poling in nonlinear crystals, we obtain the transversal grating vector $\vec{k}_g$ from the Fourier transform of the 2D index profile. For the ideal case of a uniform rectangular waveguide, k_{gx} (k_{gy}) is simply a sinc function centered at $k_{gx} = 0$ ($k_{gy} = 0$) with a half width of π/w_x (π/w_y). We note that the transverse momentum of the signal field in its fundamental waveguide propagating mode is also bounded by $|k_{sx,sy}| \leq \pi/w_{x,y}$.

The modified transverse momentum matching condition becomes

$$\vec{k}_{st} + \vec{k}_{it} + \vec{k}_{gt} = 0\,, \tag{2.16}$$

and the vectorial form allows the possibility of an asymmetric waveguide profile. The longitudinal phase-matching condition Eq. (2.13) can be written as

$$\Delta k_z = \left(k_p - k_s - k_i - \frac{2\pi}{\Lambda}\right) + \frac{C}{2k_s}, \tag{2.17}$$

$$C = k_{st}^2 + (k_{st} + k_{gt})^2 . \tag{2.18}$$

Consider the case that C is a constant over the range of possible k_{st}, which is bounded by $|k_{st}| \leq \pi/w_t$ for waveguide propagating modes. At the maximum value of $k_{st} = \pm\pi/w_t$, we have $C \geq 2\pi^2/w_t^2$. On the other hand, at the minimum value $k_{st} = 0$, $C = k_{gt}^2$. Given that k_{gt} is a sinc function that has the first zero at $\pm 2\pi/w_t$, it is always possible to find a k_{gt} for any value of k_{st} such that C is a constant. In this case, the waveguide phase-matching function of Eq. (2.17) behaves similar to the normal bulk-crystal phase matching.

Noting that the phase-matched output has no transverse wave number dependence within the k_{st} waveguide-propagating range of $\pm\pi/w_{st}$, we can now evaluate the spectral brightness of the output signal. Rewriting the angular integration over ϕ_s in Cartesian coordinates, we have

$$\int_0^{\phi_{\max}} \frac{1}{2\pi} k_s^2 \phi_s \mathrm{d}\phi_s \rightarrow \frac{1}{(2\pi)^2} \int_{-\pi/w_x}^{\pi/w_x} \mathrm{d}k_{sx} \int_{-\pi/w_y}^{\pi/w_y} \mathrm{d}k_{sy} = \frac{1}{w_x w_y} \tag{2.19}$$

The spectral brightness of the signal output is then given by

$$\frac{\mathrm{d}P_s}{\mathrm{d}\lambda_s} = \frac{16\pi^3 \hbar d_{\mathrm{eff}}^2 L^2 c P_p}{\epsilon_0 n_s n_i n_p \lambda_s^4 \lambda_i} \frac{1}{A_{\mathrm{wg}}} \mathrm{sinc}^2(\Delta k_z L/2) , \tag{2.20}$$

where $A_{\mathrm{wg}} = w_x w_y$ is the cross-sectional area of the waveguide, and Δk_z is given by Eq. (2.17). The combination of the constant $C/2k_s$ and the longitudinal grating momentum $2\pi/\Lambda$ in Eq. (2.17) yields an effective grating momentum in the waveguide $2\pi/\Lambda' = 2\pi/\Lambda + C/2k_s$ so that the sinc function dependence of the waveguide output remains the same as in the bulk crystal. The enhanced waveguide output is due to the factor $1/A_{\mathrm{wg}}$ resulting from a much larger phase-matched k_{st} range. The SPDC interaction remains phase matched within a large range of effective divergence of the

signal field because such divergence is always compensated by the transverse grating momentum k_{gt} imposed by the waveguide.

Comparing Eq. (2.20) with Eq. (2.6), our theory gives a result that is almost identical to that in Ref. [26], except that we use the waveguide cross-sectional area A_{wg} and [26] uses the field interaction area A_I. In a waveguide with relatively strong confinement, the majority of the interacting fields lie within the rectangular cross section, and A_{wg} and A_I are approximately the same. For instance, in a 4 μm×4 μm Z-cut KTP waveguide with constant $\Delta n = 0.02$ over the cross-section, we calculate the A_I for a degenerate type-II process at λ=404.8 nm to be 15.52 μm^2, implying a difference between A_{WG} and A_I of only 3%.

Our theory based on transverse momentum is physically intuitive. Naturally, the smaller the waveguide dimension, the larger the bandwidth of $\bar{k}_{gt}$ for phase matching, thus a higher SPDC efficiency could be attained. Effectively the signal and idler fields propagating non-collinearly are phase matched collinearly with the pump through compensation by the waveguide grating vector $\bar{k}_{gt}$. We note that the transverse phase matching is expected to fail as soon as k_{st} exceeds the limit of π/w_t. Hence the effective angular divergence for waveguide SPDC is

$$\phi_{wg}^{\text{div}} \simeq \frac{\pi}{wk_s} \simeq \frac{\lambda_s}{n_s w}, \tag{2.21}$$

Comparing Eq. (2.21) with Eq. (2.15), for commonly fabricated waveguides, the width w is of a few microns, whereas the length L of the crystal is of centimeters, therefore $\phi_{wg}^{\text{div}} \gg \phi_{bulk}^{\text{div}}$.

2.3 Numerical Calculations

According to our transverse momentum theory, a comparison between the waveguide and the bulk crystal case can be made more quantitative. Here we introduce an enhancement factor $\Gamma_{enhance}$, which is defined as the ratio of the SPDC emission flux in a waveguide to that in a bulk crystal. For a fair comparison, the waveguide and

the bulk crystal are of the same nonlinear material (eg. same nonlinear coefficient) with the same length, and the same order of periodic poling. The idea is that we can formulate a simple expression to estimate the waveguide SPDC pair generation rate with a known bulk crystal pair generation rate. As discussed above, the enhancement is a result of a larger angular divergence allowed in a waveguide for transverse phase-matching. Constrained to one dimension, we have already shown that $\phi_{wg}^{\text{div}} \gg \phi_{bulk}^{\text{div}}$, or

$$\frac{\phi_{wg}^{\text{div}}}{\phi_{bulk}^{\text{div}}} \simeq \sqrt{\frac{\lambda_s L}{\pi n_s w^2}} \gg 1 \tag{2.22}$$

where we have assumed a frequency degenerate SPDC output $k_s \approx k_i$. The total emission output is over a 2 dimensional space. Considering a cone of signal field emission at the output of the nonlinear crystal, given a fixed crystal length, the number of photons emitted in the cone is proportional to the base area of the cone, or the square of the radius of the cone. Following this simple argument, we conclude that the enhancement factor $\Gamma_{enhance}$ is the square of the 1-dimensional angular divergence ratio in Eq. (2.22). Therefore,

$$\Gamma_{enhance} = (\frac{\phi_{wg}^{\text{div}}}{\phi_{bulk}^{\text{div}}})^2 \simeq \frac{\lambda_s L}{\pi n_s A_{\text{wg}}}. \tag{2.23}$$

It is seen that the enhancement is inversely proportional to the waveguide cross-section area, which is consistent with our intuition. Moreover, the enhancement is proportional to the length of the waveguide. A longer waveguide leads to a narrower downconversion bandwidth, which is desirable for long-distance fiber distribution of photon pairs so as to minimize dispersion. Thus, to take full advantage of the waveguide SPDC, we should aim to fabricate a long waveguide for SPDC application.

Equation (2.22) can be of practical importance. It allows us to make a quick estimate of the waveguide SPDC flux without going through the lengthy calculation in Eq. (2.20). In the literature, reported waveguide SPDC flux at a given pump wavelength is rare, but the bulk crystal SPDC flux at any pump wavelength can be easily found. To verify the accuracy of our model and the derivation towards $\Gamma_{enhance}$, we make an example calculation of a waveguide SPDC.

Example: We compare the SPDC pair generation rates of a bulk crystal PPKTP and an ion-exchanged PPKTP waveguide. The length of the crystal is 10 mm in both cases. The pump wavelength is 405 nm. The output is type-II frequency degenerate photon pairs at 810 nm. In both cases, a first order periodic polling is implemented for the desired quasi-phase-matching. We assume that the bulk and waveguide has the same nonlinear coefficient. The waveguide channel is 4 μm wide, and it has a diffusion index profile along the vertical dimension. The depth of the waveguide can be estimated at 8 μm. The waveguide has step index profile over its cross-section.

With $L = 10mm$, $\lambda_s = 810$ nm, $n_s = 1.79$, and an approximated rectangular waveguide area of $4{\times}8$ μm^2, Eq. (2.23) yields $\Gamma_{enhance} \simeq 46$. Experimentally, Fiorentino *et al.* measured the pair production rate to be $\sim 7.3 \times 10^7$ pairs/s/mW of the pump for the same waveguide described above. In addition. they reported a 10 mm PPKTP bulk crystal pair production rate to be 1.5×10^6 pairs/s/mW of the pump over the aggregate band. Thus the experimentally measured enhancement factor is ~ 49. It is clear that our estimate of ~ 46 fold enhancement is in very good agreement with experimental results. This example verifies that our transverse momentum theory on waveguide SPDC gives a reasonable explanation for the enhanced efficiency.

Finally, it is useful to estimate the SPDC flux of our waveguide photon pair source based on the transverse momentum theory we developed in this chapter. We operate the waveguide using a continuous-wave pump laser at λ_p=658 nm, so the type-II frequency degenerate output is at $\lambda_{s,i}$=1316 nm. Critical specifications of our PPKTP waveguide are described in detail in the next chapter. Its transverse index profile is the same as the waveguide mentioned in the above example. For first order approximation, we have $A_{WG} \simeq 32.0$ μm^2. The length of our waveguide is L=16 mm. The mode indices for the pump, signal and idler photon are estimated at

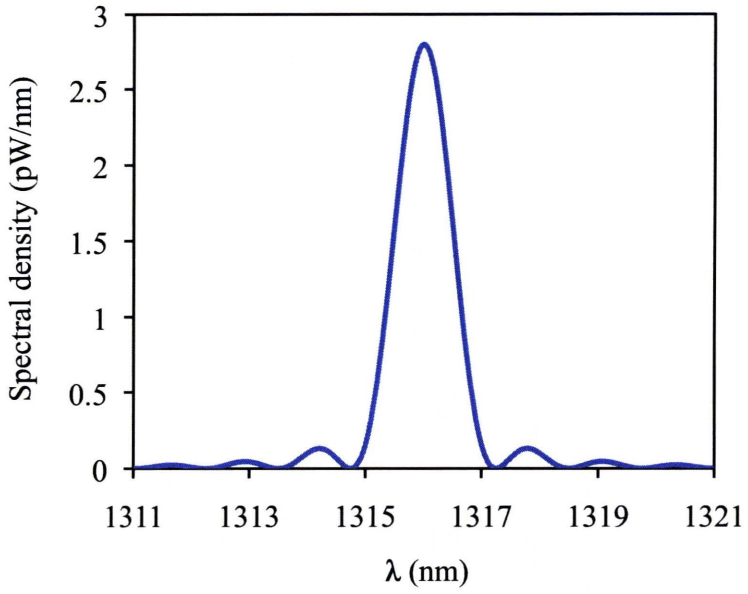

Figure 2-2: Theoretical signal spectral power density of the PPKTP waveguide with 1 mW pump power calculated from Eq. (2.20).

$n_p = 1.783, n_s = 1.749, n_i = 1.830$, respectively. We assume the effective nonlinear coefficient to be the same as that in PPKTP bulk crystal $d_{eff} = 2.1$ pm/V. Using Eq. (2.20), we calculate the pair generation rate of our waveguide source to be $\sim 2.1 \times 10^7$ pairs/s/mW of pump power over the entire band. The calculated spectrum of the signal photon is plotted in Fig. 2.3. We see that the spectrum looks the same as the single-spatial-mode output of a bulk crystal, except that the spectral power density, defined as pW/nm/mW of the pump, is much larger than that in the bulk case. Here we calculate the peak spectral power density of our waveguide to be 2.8 pW/nm/mW of the pump. The phase matching bandwidth, which is defined as half the zero-to-zero width of sinc-squared function, is estimated at 1.1 nm. The high brightness and narrow bandwidth of our waveguide output is well suited for efficient generation of polarization-entangled photons for long-distance fiber distribution.

Chapter 3

Specifications of Fiber-Coupled PPKTP Waveguide

3.1 Fabrication and Packaging

The PPKTP waveguide was fabricated by AdvR inc. The information and the picture presented are this section is provided by Tony D. Roberts and Philip Battle from AdvR inc.. The PPKTP waveguides were fabricated on a flux grown, z-cut KTP wafer. A direct contact mask designed for 4 mm wide channel waveguides was used to pattern a layer of Al onto the +z surface of the wafer. The wafer was diced into 3 mm $\times$ 10 mm chips and polished on the optical surfaces. The chips were placed in a molten bath of $RbNO_3$ salt at $400^{\circ}C$ for 120 minutes. The bare areas of the patterned surface underwent ion exchange in which Rb+ ions diffused into the KTP, replacing K+ ions to a depth of around 8 μm, forming an index step relative to the surrounding KTP. After ion exchange the Al layer was removed, and the chip was annealed in air at 325° C for 15 minutes. The waveguides were periodically poled using an electrode on a separate glass substrate placed in contact with the KTP surface. The electrode was fabricated using contact lithography to define a chrome grating pattern with a period of 227 μm. The patterned electrode was aligned and pressed to the +z surface; a ground electrode consisting of a uniform metal substrate contacted the -z surface. The poling waveform was applied using a Trek 20/20C high

voltage amplifier controlled by a computer program that simultaneously monitored the electrode current.

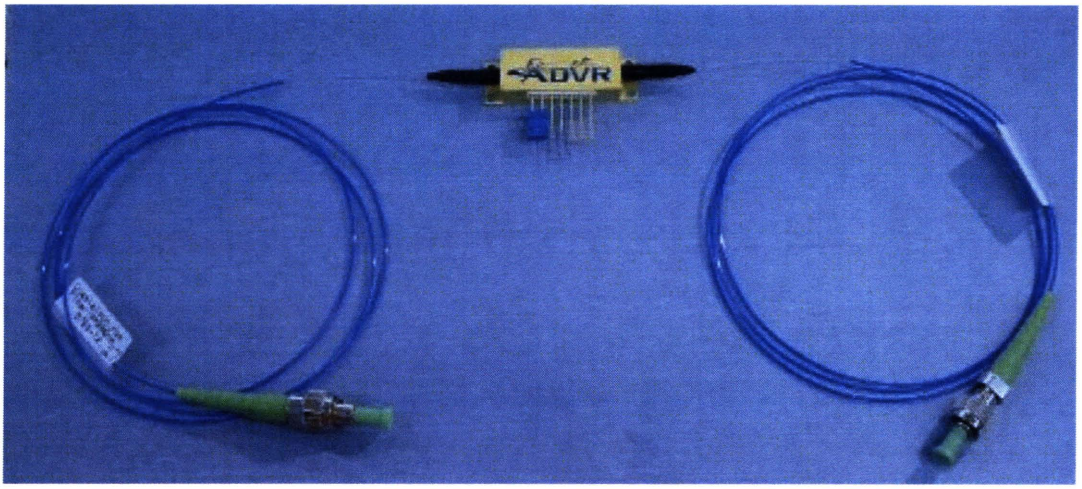

Figure 3-1: A picture of the fiber-coupled PPKTP waveguide package fabricated by AdvR inc.

The fabricated PPKTP waveguide was 1.6-cm long. The resultant transverse index profile had a 4-μm wide index step of 0.02 in the lateral direction, and a diffusion profile along the Z direction as $n(z) = n_{KTP} + 0.02\exp(-z/d)$, with d = 8 μm. For a type-II process, the pump field is polarized along the crystallographic Y axis, while the signal and idler fields are polarized along the crystallographic Y and Z axes, respectively. All fields propagated along the X axis of the crystal. The waveguide was periodically poled with a grating period of 227 μm, designed for type-II quasi phase matching (QPM) with frequency-degenerate outputs at 1316.0 nm around room temperature. We used the Sellmeier equation of bulk KTP [40] and the finite difference approximation [41] to calculate the eigenmodes of the waveguide. The mode indices for the pump, signal and idler fields are estimated to be $n_p = 1.783, n_s = 1.749, n_i = 1.830$, respectively. Finally, polarization maintaining (PM) fibers were attached to the waveguide optically polished facets for pump input and downconversion output. The fiber to waveguide coupling efficiency was ~50% at room temperature for the output fiber (Coastalcon PM1310), and was ~49% for

the input fiber (Coastalcon PM630). The fiber-coupled module was packaged into a encapsulation of dimension 20 mm×10 mm×5 mm. A four-pin electrical interface allowed connection to the built-in thermoelectric cooler (TEC) and a 10kΩ thermistor. A picture of the packaged waveguide device is shown in Fig. 3-1.

3.2 Fundamental Mode SPDC

The waveguide source was designed to operate in the fundamental waveguide modes. According to the theory of Eq. (2.20), SPDC flux is maximum for the fundamental pump, signal and idler modes, because these modes contribute to the tightest confinement and the smallest effective overlap area A_I. Moreover, the coupling of light between the waveguide and single mode fibers is optimized for the fundamental pump mode being excited, and the fundamental downconverted modes being coupled out of the waveguide, because these modes most closely resemble the shape of the Gaussian profile in their respective fibers. The finite difference scalar approximation method was used to efficiently simulate the electric field distributions of the pump, signal and idler fundamental modes. Fig. 3-2 illustrates the profile of the pump fundamental mode. In this figure, we also indicate the waveguide top surface and the edge boundaries of the diffusion zone in blue lines. The calculated field is normalized and re-scaled so that the peak field intensity corresponds to a value of 256 in the color map.

It is seen that the pump mode is compact, occupying an area of ~4×4 μm^2, and it is close to a symmetric circle in shape. The majority of the field is confined with in the diffusion zone, which suggests that $|k_{sy}| \simeq \pi/w_y$, therefore our modeling using a transverse momentum theory in chapter 2 is valid. The peak intensity is located ~1.5 μm below the crystal top surface, and it is where the center of the pump fiber was butted to the waveguide input facet.

We performed the same calculation for the signal and idler fields, which are plotted in Fig. 3-3. Given the symmetry of the waveguide structure, we only plot half of the crosssection. At longer wavelengths, the mode is expected to occupy a larger area.

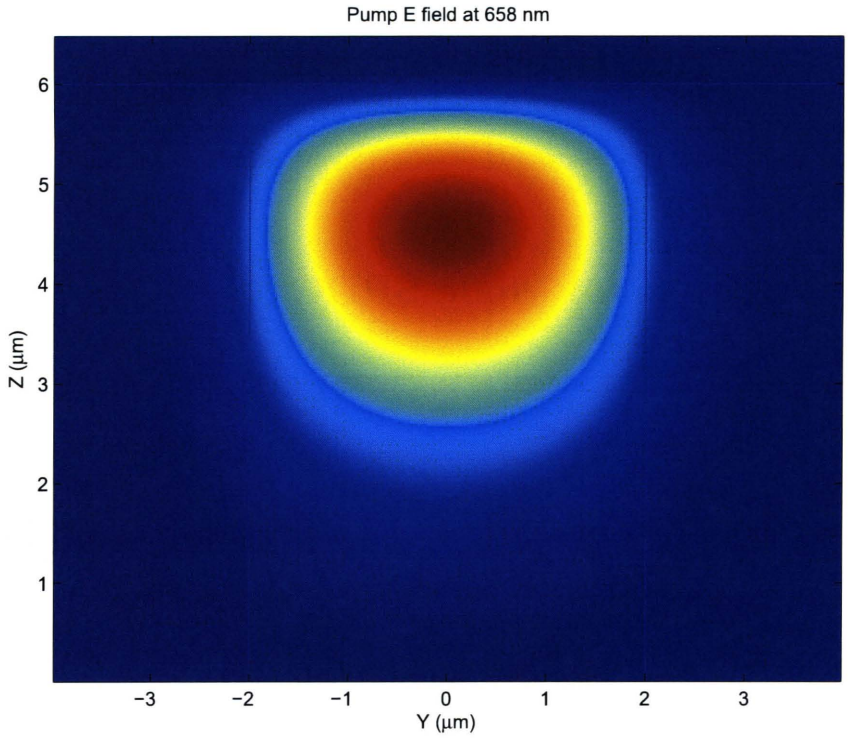

Figure 3-2: Plot of the fundamental eigennmode for pump electric field. The blue lines indicate the top surface of the crystal (horizontal line) and the edge of the diffusion profile zone (vertical lines). The scale is linear and ranges from 0 to 256. A finite difference scalar approximation was used to solve the eigenmode problem.

In this case, both signal and idler modes extend over an area of $\sim 4 \times 8\ \mu m^2$, almost twice the pump mode. The peak intensity is located $\sim 2.5\ \mu m$ below the top surface for both signal and idler, so that was the position where the center of the IR fiber was butted to the waveguide output facet. We note that the modes are still well confined within the diffusion zone, but they are elongated in the Z direction. This effect is a result of our diffusion index profile along the Z axis, instead of a perfect index step.

The knowledge of mode profiles allows an easy calculation of the effective mode overlap area. For the combination of three fundamental modes, we have A_I=27.9 μm^2. This value can be compared to the diffusion zone area of $\sim 4 \times 8\ \mu m^2$, which is $A_{wg} = 32 \mu m^2$. Note that the two numbers are very close, which is due to the fact that all three modes are reasonably confined within the diffusion zone. Consequently, the

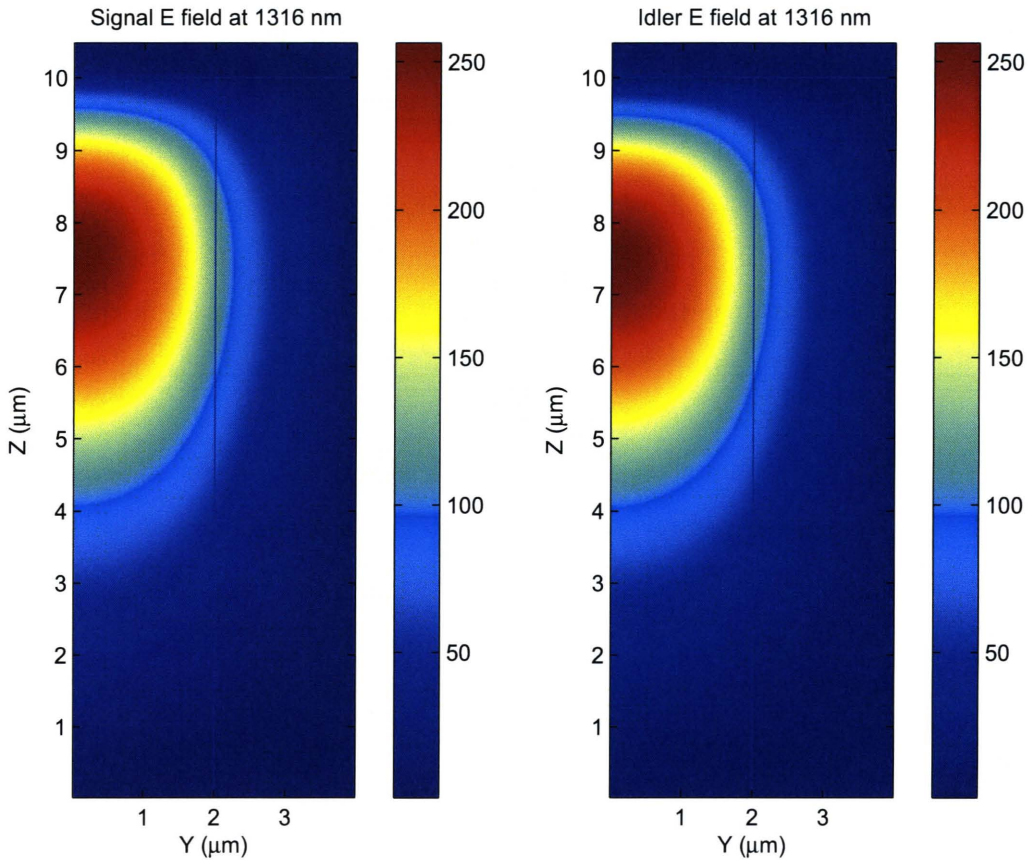

Figure 3-3: Plot of the fundamental eigennmodes for signal and idler electric fields. Only half of the structure has to be simulated given the problem symmetry.

theoretical estimations of the waveguide SPDC flux using two area definitions will not lead to a significant difference. The small discrepancy is a result of our simplification in the theory, where we assumed that the pump is a plane wave propagating along the waveguide. Nevertheless, for simplicity, we will adopt the value of A_{wg} in our calculation regarding the waveguide SPDC flux.

3.3 Higher-order Mode SPDC

The fabricated PPKTP waveguide can support multi-spatial modes. Even though those higher-order spatial modes are not designed to contribute to the waveguide

SPDC output, we are still interested in the effects of different combinations of the pump, signal and idler spatial modes for the following reasons. First, there is a finite area overlap between the waveguide higher-order modes and the mode of a fiber. All orders of waveguide eigenmodes are orthogonal to each other, but due to their lack of circular symmetry, neither of them is completely orthogonal to the Gaussian mode of a single mode fiber. Second, the alignment of the fiber to the waveguide could change with temperature, which may cause the higher-order modes to be excited. In experiments, we have observed that the coupling efficiency between the fiber and the waveguide changed when we tuned the waveguide temperature. The changed coupling manifested as a dramatic decrease in the residue pump power coming out of the IR output fiber. Such misalignment might be caused by the different thermal expansion coefficients of the fiber and the KTP crystal.

Because the fiber coupling is permanent, we could not fully characterize the higher-order modes or have a way to control them. But the presence of higher-order modes in SPDC can be a problem in our measurements. Excitation of higher-order modes of the pump reduces the power countable in the fundamental mode. The result is a lowered SPDC flux as compared to the theoretical value. If higher-order mode excitation is strong, the flux reduction in SPDC output can be so severe that the waveguide output flux is not much higher than that in a bulk device. Additionally, higher-order SPDC output spectra might be present within the phase-matching bandwidth of the fundamental mode SPDC, causing an increased amount of noise (uncorrelated photons) for photon pair generation. The higher-order modes generally have different effective mode indices and dispersion properties from those of the fundamental mode, so their SPDC spectra are expected to be different from each other. To investigate the spectral distribution of the possible higher-order mode SPDC, we require some detailed knowledge of their mode profiles.

The field profiles for the four lowest order eigenmodes are illustrated in Fig. 3.4 for the pump, in Fig. 3.5 for the signal, and in Fig. 3.6 for the idler, respectively. The scales in those figures are the same as that in Fig. 3-3. We denote TE mode as having an electric field polarization along the Y axis, and TM mode as having an electric

field polarization along the Z axis. Thus the pump and the signal are in TE mode, whereas the idler is in TM mode. Each spatial mode can be addressed by using a pair of indices, one for the spatial order in Y direction, and the other for Z direction. The fundamental mode is labeled as $\{00\}$, and the next higher order modes are $\{01\}$ and $\{10\}$, for example. The four lowest order modes shown in Fig. 3.4, 3.5, 3.6, excluding the fundamental mode, are $\{01\}$, $\{10\}$, $\{02\}$, and $\{11\}$ modes. The effective indices for the above-mentioned modes were calculated at their respective wavelengths, and we list them in Table 3.1.

Waveguide Spatial Mode Effective Index		
Field (wavelength)	Eigenmode	Effective index
Pump (658 nm)	TE01	1.77944
	TE10	1.77957
	TE02	1.77360
	TE11	1.77599
	TE20	1.77702
	TE30	1.77486
	TE21	1.77362
Signal (1316 nm)	TE01	1.73973
	TE10	1.74427
	TE02	1.72731
	TE11	1.73534
	TE20	1.73840
	TE30	1.73007
	TE21	1.72943
Idler (1316 nm)	TM01	1.82049
	TM10	1.82480
	TM02	1.80842
	TM11	1.81617
	TM20	1.81907
	TM30	1.81094
	TM21	1.81041

Table 3.1: Effective indices of the waveguide higher-order eigenmodes at the pump wavelength and the signal, idler wavelength. Eigenmodes are labeled by a pair of index representing the spatial orders in two dimensions.

Each combination of the pump, signal and idler eigenmodes could contribute to an independent SPDC process. When at least one of the three interacting fields is not in the fundamental mode, we call this combination a higher-order SPDC process. Since each mode has its distinct effective index and dispersion property, every higher-order SPDC process fulfills the phase matching condition differently. The location of the output spectra and the bandwidths of the downconverted photons are unique to a specific combination, allowing us to identify the individual processes in the final SPDC spectrum. The SPDC flux or the spectral density contributed by each combination of modes could be vastly different. First, the effective overlap area A_I, as we defined in chapter 2, is different for each process. Higher-order modes generally extend more into the surrounding non-diffusion zone, so they occupy a larger area, and the SPDC flux is smaller accordng to Eq. (2.20). Second, those higher-order modes are, if possible, only weakly excited. In our fiber-coupled device, the single mode fiber essentially serves as a spatial mode filter. We expect that the majority of the power is coupled into the waveguide fundamental mode, and higher-order modes can only be slightly excited. A similar situation happens at the output end of the waveguide, where only the fundamental mode can be coupled efficiently into the fiber, with most of the higher-order modes filtered out by the single-mode fiber.

Among all the combinations, what particularly concerns us is the set of higher-order SPDC processes that are phase matched in the same band as the fundamental SPDC. The spectrum of each process is fully characterizable by the corresponding sinc-squared phase matching function, with a Δk mismatch given by Eq. (2.10). In principle, there are infinite number of modes, and the probability for finding a specific combination to be phase matched near 1316 nm increases as we include modes of higher orders into consideration. However, in reality, most of the high-order modes are unexcited, or their effects are too small to be observed. So we can concentrate on the lowest order modes for each field; for instance, those modes whose spatial index is less than or equal to 2. We performed the same mode profile simulation over the wavelength range, and calculated the phase matching function for a few combinations of the three interacting modes. The results are listed in Table 3.2. For simplicity, we

denote a higher-order SPDC by writing $\{jk\} \longrightarrow \{mn\} + \{pq\}$, where we drop the TE, TM label, and the three pairs of indices refer to pump, signal and idler from left to right.

Possible Waveguide SPDC Process		
Pump⟶Signal+Idler	Signal wavelength	Idler wavelength
00⟶00+00	1316	1316
11⟶11+00	1310.2	1321.9
11⟶00+11	1304.9	1327.3
11⟶01+10	1312.5	1319.5
11⟶10+01	1315.8	1316.2
20⟶20+00	1294.2	1338.5
20⟶00+20	1293.4	1339.4
02⟶30+00	1314.1	1317.9
02⟶00+03	1311.8	1320.2

Table 3.2: List of possible combinations of lowest order modes for waveguide SPDC process, and their respective signal and idler photon wavelengths when the waveguide is pumped by a cw 658 nm laser and is phased-matched for degenerate fundamental mode output at 1316 nm.

For the calculation, we assume a cw pump at 658 nm, and the fundamental output are frequency degenerate at 1316 nm. Hence we only look at the possible SPDC processes which result in a phase-matched signal or idler wavelength within the band of 1290 nm to 1340 nm. The cases outside this band are ignored because they are too far from the wavelength of interest. For our fiber-coupled waveguide design, a single mode operation is important, thus all processes other than the fundamental SPDC need to be suppressed. The possible processes listed in Table 3.2 can be categorized into three kinds. The first kind include those with signal or idler wavelength $\geq$5 nm away from 1316 nm: 11⟶11+00, 11⟶00+11, 20⟶20+00, 20⟶00+20. They can be readily isolated from the fundamental process using a 10-nm bandwidth band-pass filter. The second kind are those with signal and idler spectra adjacent to 1316 nm: 11⟶01+10, 02⟶30+00, 02⟶00+03. These processes can still be removed of by using a narrowband filter of bandwidth about $\sim$1 nm, The last one

is 11$\longrightarrow$10+01 whose output spectrum overlaps with the 00$\longrightarrow$00+00 process. In this case, it can not be isolated by using spectral filtering. We note that the effective overlap area corresponding to this particular combination is A_I=267.5 μm^2, which is $\sim$10 times larger than the overlap area of the fundamental SPDC. Therefore, according to Eq. (2.20), the SPDC flux per unit pump power is $\sim$10 times smaller. We suspect that with the spatial filtering effect of the fiber, we will not see a significant amount of SPDC output produced by this 11$\longrightarrow$10+01 process. Overall, we conclude that with proper spectral filtering using band-pass filters, our waveguide source can be operated free of any higher-order SPDC process.

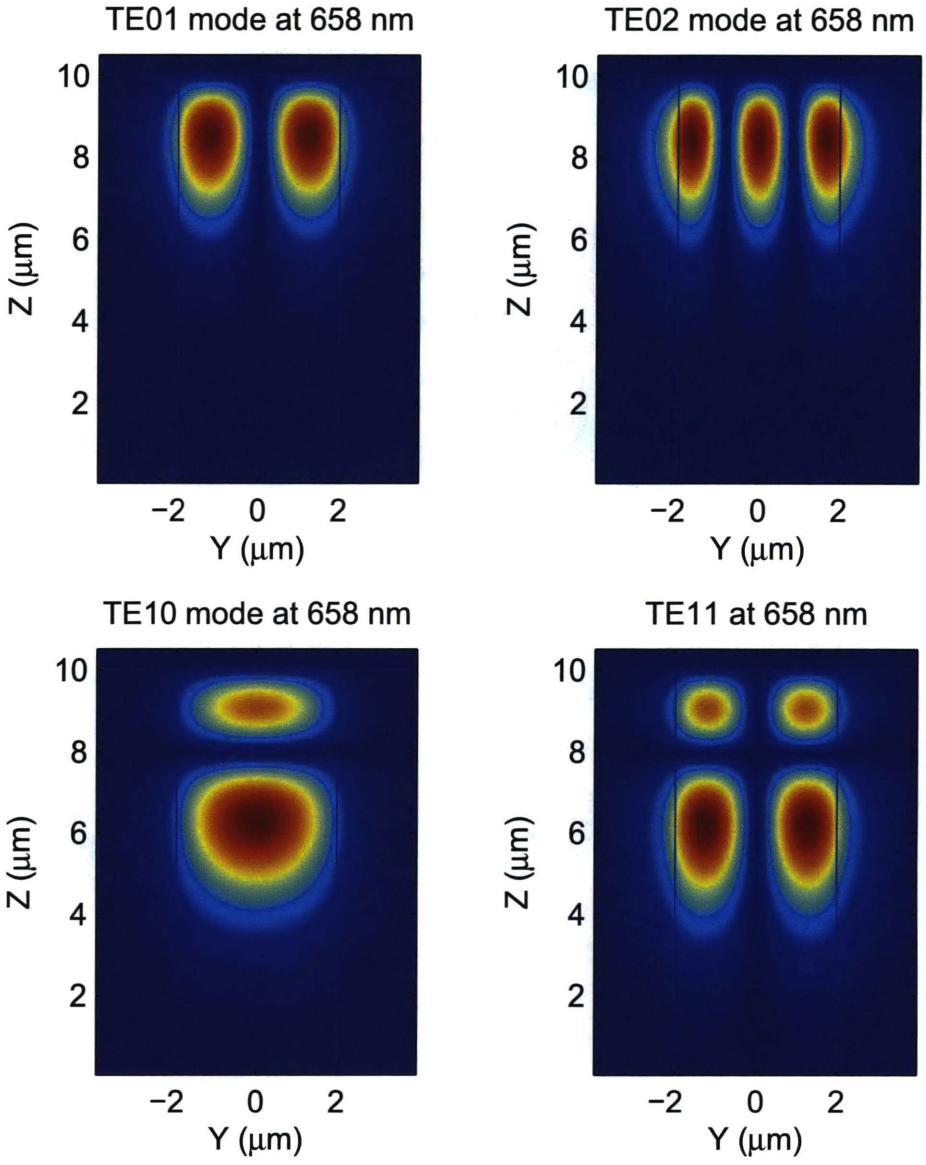

Figure 3-4: Plots of the four lowest order (beside the fundamental mode) eigenmodes for the pump field. The eigenmodes are TE01, TE02, TE10, TE11 mode, where TE refers to the polarization along the Y axis.

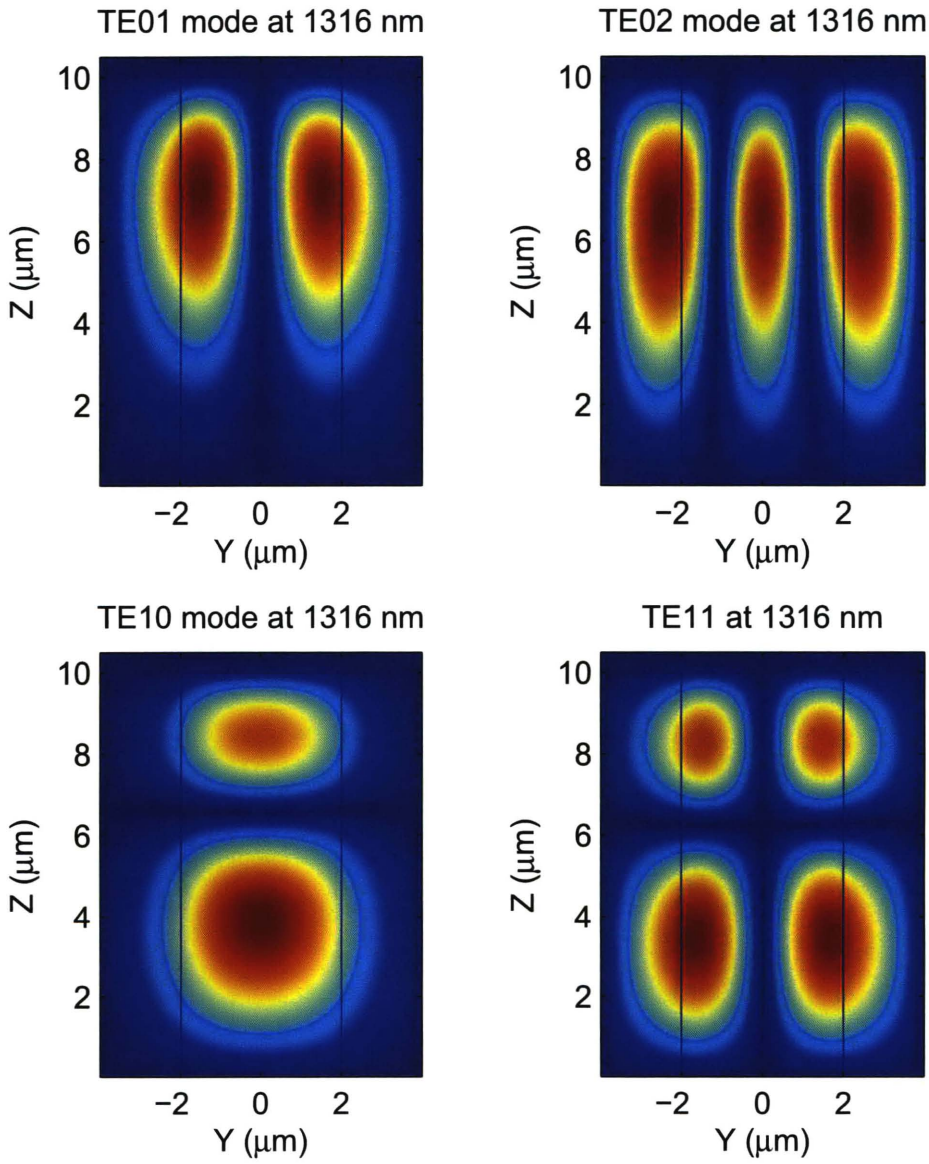

Figure 3-5: Plots of the four lowest order (beside the fundamental mode) eigenmodes for the signal field. The eigenmodes are TE01, TE02, TE10, TE11 mode, respectively.

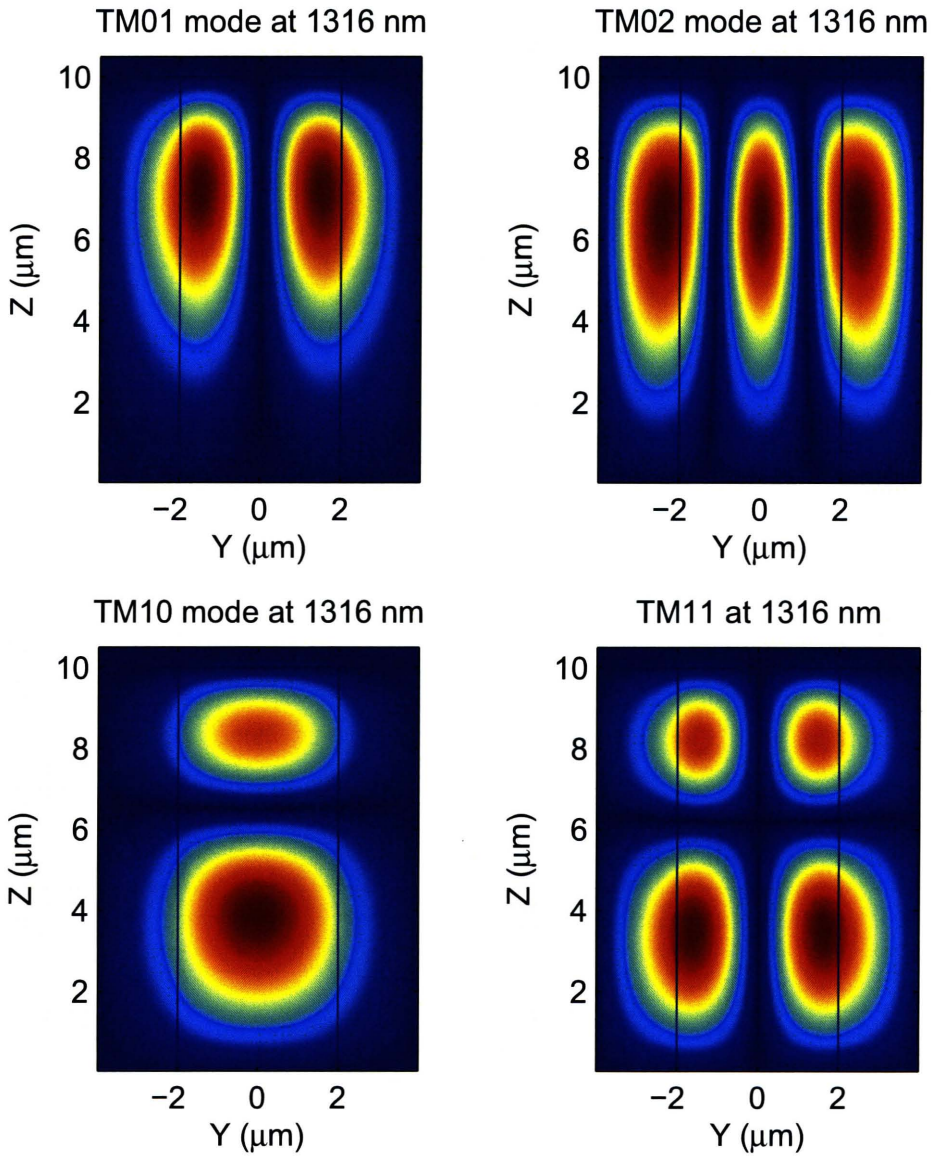

Figure 3-6: Plots of the four lowest order (beside the fundamental mode) eigenmodes for the idler field. The eigenmodes are TM01, TM02, TM10, TM11 mode, respectively.

Chapter 4

Flux and Spectrum Characterization

4.1 SHG Characterization

In our preliminary characterization, we measured the type-II second harmonic generation (SHG) process inthe PPKTP waveguide device. The experimental setup for the SHG measurement is shown in Fig. 4.1. A fiber-coupled diode laser at 1.31-μm was modulated by a 10 kHz reference signal, and was collimated for free space output. The laser light was sent through a polarizing beam splitter (PBS) and a half-wave plate (HWP) before it was focused into the infrared polarization maintaining fiber (PMF) of our waveguide device. The orientations of the PBS, the HWP and the PMF were set up such that the transmission axis of the PBS was aligned with the slow axis of the PMF, and the HWP was rotated 22.5° with respect to the PBS. This arrangement set the SHG fundamental wave at a polarization 45° relative to the crystallographic Y axis of the PPKTP waveguide, so there were equal input powers along the crystallographic Y and Z axes. The polarization of the laser light was adjusted by a fiber polarization controller, such that maximum laser power could transmit through the PBS. The remaining laser light reflected by the PBS was monitored using an optical power meter. The SHG output at ~657 nm was collimated and detected by a Si PIN photodiode. The photodiode output RF signals were first filtered by a band-pass fil-

ter, and were sent to a lock-in-amplifier. The lock-in-amplifier was initially calibrated against the absolute SHG output, and was used to measure the relative SHG power as we tuned the fundamental input wavelength or the waveguide temperature.

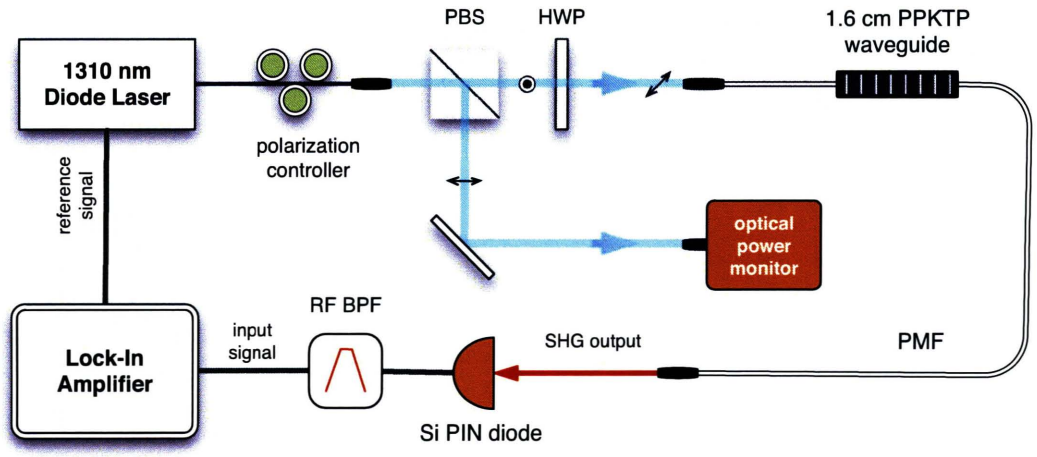

Figure 4-1: Experimental setup for second harmonics generation measurement on the PPKTP waveguide. PBS: polarizing beam splitter; HWP: half wave plate; PMF: polarization-maitaining fiber; RF BPF: radio frequency band-pass filter.

With the waveguide temperature fixed at 23.5° C, we tuned the wavelength of the diode laser and recorded the voltage output from the lock-in-amplifier. Fig. 4.2 plots the relative SHG output power against the fundamental input wavelength. Measurements at wavelengths larger than 1316 nm were not taken, because the diode laser we used could not be tuned beyond 1316 nm. Nevertheless, half of the SHG output bandwidth and a spectrum peak can be easily identified in Fig. 4.2. The peak indicates that the process was phase matched for 1315.6 nm at 23.5° C. In Fig. 4.2, we also plot the theoretical SHG spectrum by using the following empirical expression,

$$P_{SHG}(\lambda_f) = A\text{sinc}^2(\Delta k_{SHG}(\lambda_f)L/2) \tag{4.1}$$

$$\Delta k_{SHG}(\lambda_f) = \frac{2\pi}{\lambda_f}(2n_p(\lambda_f/2) - n_s(\lambda_f) - n_i(\lambda_f)) - \frac{2\pi}{\Lambda'} \tag{4.2}$$

where Λ' is the poling period at this particular temperature. Here we set the value of Λ' such that $\Delta k_{SHG}(\lambda_f) = 0$ at λ_f=1315.6 nm. Since our fiber-coupled waveguide

operated dominantly in fundamental modes, n_p, n_s, and n_i were the fundamental mode indices for the SPDC pump, signal and idler fields, respectively. A in Eq. (4.1) is a scaling factor used to fit the measured SHG power. We see from Fig. 4.2 that the experimental result is in excellent agreement with the theoretical prediction, which is based on the modal dispersion properties of our PPKTP waveguide. The half width zero-to-zero bandwidth of the SHG spectrum is estimated to be ~ 1.9 nm.

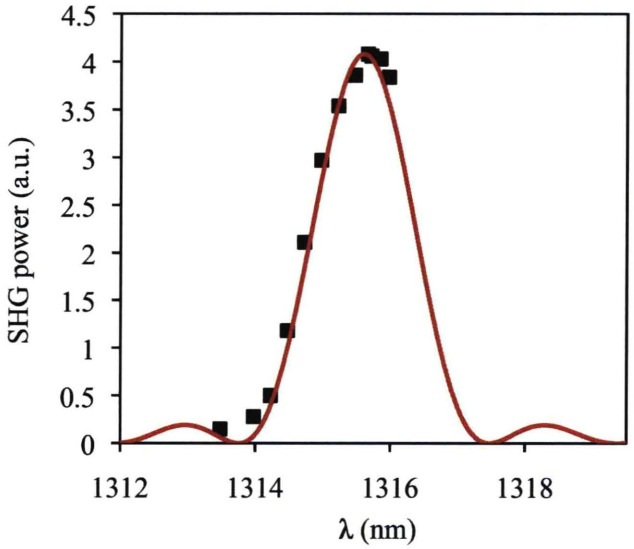

Figure 4-2: Measured relative SHG power versus fundamental input wavelength. The solid theoretical (red) curve is calculated based on the modal dispersions of the fundamental and SHG fields in the PPKTP waveguide.

Next, we repeated the SHG spectrum measurement at different waveguide temperatures. For each temperature, we found the corresponding fundamental input wavelength at which peak SHG power occurred. The experimental results are shown in Fig. 4.3, which plots the phase-matched fundamental wavelengths against the waveguide temeperature. The linear fit of the measured data yields a phase-matched temperature tuning curve. The estimated SHG temperature tuning coefficient is

$$\frac{\mathrm{d}\lambda_{phm}}{\mathrm{d}T_{wg}} \simeq 0.15 nm/^{\circ}\,\mathrm{C} \tag{4.3}$$

This value is comparable to that of the bulk KTP crystal [42], and is significantly

smaller than the temperature tuning coefficient of other common nonlinear materials, such as PPLN[43]. A small temperature tuning coefficient is highly desired for applications like polarization entanglement generation. It means the photon pair source can tolerate relatively large temperature fluctuations, and yet maintain a highly frequency-degenerate signal and idler outputs. In our experiment, we observed that even without an active control of the waveguide temperature, the signal and idler spectra at room temperature overlapped, with the two spectra peaks separated by <0.5 nm. Using a temperature controller, which has a temperature resolution of 0.1° C, we could easily obtain the degenerate two-photon spectra with a spectral peak separation stablized at <0.015 nm. This high degree of frequency degeneracy, together with narrowband filtering, made the spectral overlap between the signal and idler photons virtually perfect in our experiment. Lastly, the obtained phase matched tuning curve confirms that the degenerate signal and idler at 1316.0 nm occurred in the room temperature range.

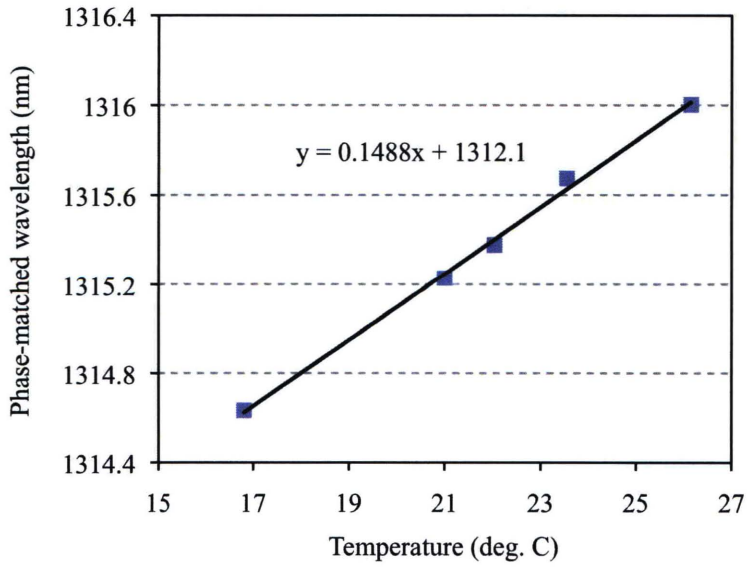

Figure 4-3: Phase-matched tuning curve for second harmonics generation in the PPKTP waveguide, with a linear fit function.

The nonlinear coefficient of the PPKTP waveguide can be determined from an

absolute power SHG measurement. For the experimental setup in Fig. 4.1, the output of the lock-in-amplifier was initially calibrated, so the absolute SHG power could be readily obtained from the amplifier reading. At the input end, the fiber to fiber coupling efficiency, including the transmission through the PBS and HWP, was separately measured at ~80%. There was a small amount of laser power reflected by the PBS, and was detected by the optical power meter. Such leakage power was subtracted from the total laser output in estimating the true fundamental input power in the waveguide. By taking into account the ~50% coupling efficiency between the PMF and the waveguide, we estimated a fundamental input power of 3 mW, with P_{in}=1.5 mW for each polarization. Under this input, we measured the SHG output to be P_{out}=67 nW at a phase matched SHG spectral peak. The waveguide SHG process has been extensively studied in the literature. Assuming the fundamental input is non-depleted, then the waveguide SHG efficiency is given by [44],

$$\eta_{SHG} = \frac{P_{in}}{P_{out}} = \kappa^2 L^2 P_{in} \mathrm{sinc}^2(\Delta k_{SHG} L/2) \tag{4.4}$$

where L is the length of the waveguide, and κ is the coupling coefficient for the waveguide SHG, defined as,

$$\kappa = \sqrt{\frac{(2\omega_f)^2}{2n_s(\omega_f)n_i(\omega_f)n_p(2\omega_f)}(\frac{\mu}{\epsilon_0})^{\frac{3}{2}}\frac{d_{eff}^2}{A_I}} \tag{4.5}$$

In Eq. (4.5), ω_f is the angular frequency of the fundamental field, d_{eff} is the effective nonlinear coefficient, and A_I is the effective three-mode overlap area we introduced in chapter 2. The mode indices and mode profiles of the fundamental input fields and SHG output field were calculated in chapter 3. The effective overlap area at our operating wavelength is A_I=27.9 μm^2. Since the SHG output was measured at the center of the phase matching function, we have in this case $\Delta k_{SHG} = 0$, thus the sinc-squared phase matching function was evaluated at unity. The above results, together with Eq. (4.4-4.5), allow us to calculate the relevant nonlinear coefficient $d_{eff} = 2d_{24}/\pi = 2.05$ pm/V where $d_{24} = 3.23$ pm/V. Note that the value we obtained

is consistent with previously reported nonlinear coefficient of KTP crystal [40].

4.2 Flux Characterization

Our theoretical model of SPDC in a waveguide was given in chapter 2. The measured d_{eff} using SHG allows a straightforward comparison between the theoretically estimated pair generation rate and the experimentally characterized brightness of our waveguide SPDC source. The experimental setup for characterizing the waveguide SPDC output flux is shown in Fig. 4.4. Pumped by a continuos-wave diode laser at 658.0 nm, the fiber-coupled SPDC outputs were collimated for free space output having an approximate beam diameter of 2.0 mm, and they were sent through a long-pass filter to block the residue pump. Then we used a 10-nm band-pass filter centered at 1316.0 nm to remove the fluorescence photons outside our interested band. We noted that without this band-pass filter, the measured number of fluorescence photons could be as high as 10 times the number of down-converted photons. However, by adding this filter, the fluorescence photon flux appeared to be much less than the downconverted photon flux. We chose a broadband filter of 10 nm so that both the signal and idler spectra are within the band, no matter they are at exact degeneracy or not. After the broadband filtering, we used a PBS to separate the orthogonally polarized signal and idler beams and coupled them into their respective SMF-28 single-mode optical fibers. The mode field diameter of the SMF-28 fibers was 9.5 μm at 1310 m. The fiber to fiber coupling was optimized by using a pair of matched fiber collimation packages, made of two anti-reflection coated aspherical lenses with effective focal lengths of 11.0 mm. We used a pair of flat mirrors in each channel to steer the beam into optimal focusing. At the end, we achieved reasonable coupling efficiencies of 60% and 75% for the signal and idler channel, respectively. The difference between the two channels was likely due to the wave-front distortion through the PBS. The signal and idler counts were measured using a pair of fiber-coupled InGaAs avalanche photodiode (APD) single-photon counters. The characterizations and properties of these two InGaAs APDs were reported elsewhere [46]. They operated in the Geiger

mode with a gating frequency of 50 kHz, and a 20-ns duty in each cycle. Detector efficiencies were calibrated using a laser source at 1316 nm and a fiber variable attenuator to be 15.4% and 20.5%. The corresponding dark counts were ~32.1 kHz and ~17.2 kHz, respectively. Table 4.1 lists the transmissions of each optical component for both signal and idler channels. Taking into account the waveguide-to-fiber coupling, transmission efficiencies of optical components, the overall signal and idler detection efficiencies were estimated at $\eta_s \simeq 0.9\%$ and $\eta_i \simeq 1.4\%$.

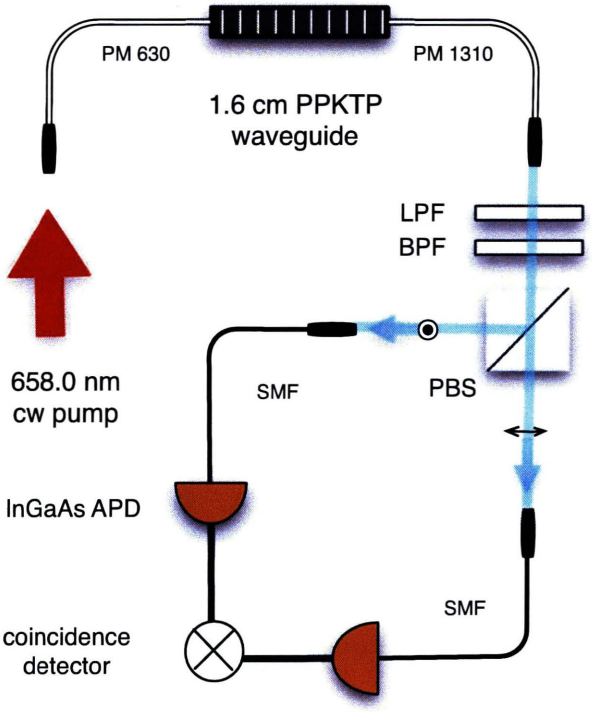

Figure 4-4: Experiment setup for characterizing the SPDC output flux of the PPKTP waveguide. LPF: long-pass filter; BPF: band-pass filter; PBS: polarizing beam splitter; SMF: single mode fiber; APD: avalanche photodetector.

The coincidence between signal and idler photons was measured using a homemade coincidence detection circuit [47]. The coincidence detector allowed a variable time coincidence window by using different lengths of electrical delay cables. When two photodetection events were separated in time less than the coincidence window,

System component transmissions		
	Signal channel	Idler channel
Waveguide to fiber coupling	50%	50%
Long-pass filter	40%	40%
10 nm Band-pass filter	50%	49%
Fiber to fiber coupling	60%	75%
Fiber connectors	95%	93%
Detector efficiency	15.4%	20.5%
Overall detection efficiency	0.9%	1.4%

Table 4.1: Optical component transmissions and the overall detection efficiencies for both the signal and the idler channel.

a successful coincidence count was registered by a PC-installed electronic counter (NI PCI-6602). In our experiments, the coincidence window was set at 2.5 ns. This choice of time window took into account the worse case jittering of the electronics to ensure that coincidences of all legitimate pairs were correctly counted. Given that since the InGaAs APDs were operated with a gating frequency of 50 kHz, the maximum coincidence counts detectable is 50k counts/s. In reality, the coincidence counts were orders of magnitude less due to the low system detection efficiencies. In fact, this specific implementation of coincidence detection had 30 dB intrinsic loss in terms of coincidence counts, because in every second only one thousandths of the time the APDs were active. The result is that our measured coincidence rates appeared in the range of 0.1 Hz to 1 Hz. Note that our gating frequency of the InGaAs APDs was lower than some state-of-art InGaAs systems [48, 49], which usually operated in the 100 kHz and 1 MHz range. The reason is that our InGaAs APDs showed significant amount of after-pulses when operated at high frequencies. The previous characterization [46] indicated that to be free from after-pulsing effect, one had to limit the gating frequency to <200 kHz. This slow detection speed inevitably resulted in a long data acquisition time and compromised measurement accuracy. To overcome the poor accuracy, for each data point we used an acquisition time in the range of 10 s to 100 s, so that there were sufficient counts in every measurement to form the photon statistics. We present the coincidence counting measurement results by normalizing

the data in units of counts/s. For example, if our system registered 3 counts in 1-s duration, the normalized detected coincidence rate is 3000 counts/s, because the actual detector operating duration is given by the gating frequency (50kHz) multiplied by the gate duration of 20 ns . Same normalization is also applied to singles counts measurement.

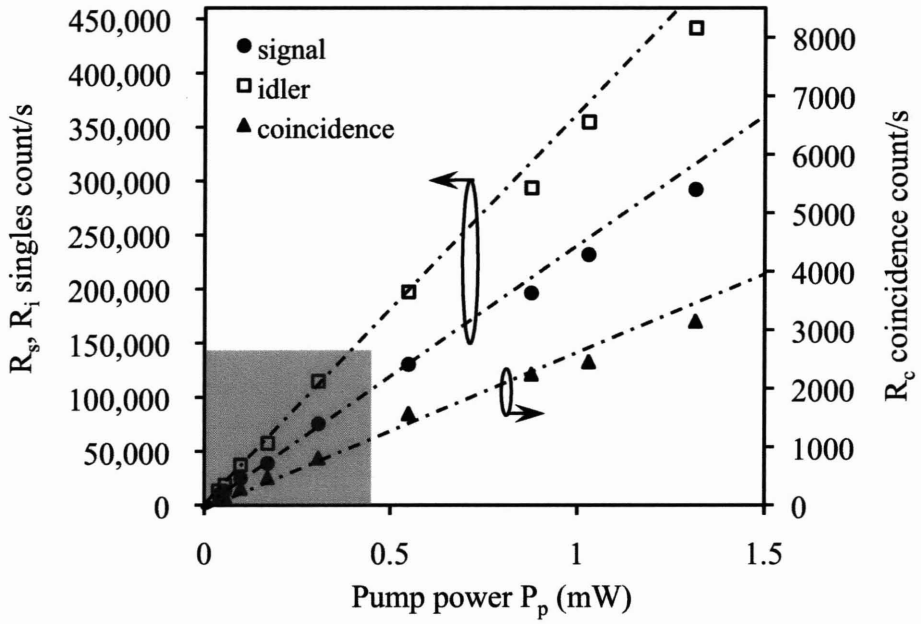

Figure 4-5: Measured singles counts (dark counts subtracted) for signal, idler, and coincidence counts (accidentals subtracted) versus pump powers. Shaded area is the region of interest in which detector saturation is negligibly small.

Fig. 4.5 shows the experimental results of our signal-idler coincidence measurement. We recorded the detected singles and coincidences rates at various pump powers P_p in the waveguide. For each pump power, accidental coincidence counts were measured by separating the gating signals for both detectors by more than 20 ns so that the coincidence events are guaranteed to be from independent photons. The induced optical delay was compensated at the coincidence circuit by using appropriate lengths of coaxial cables in order to simultaneously bring the time-separated counting events to the coincidence detector. The accidental coincidence counts were

then subtracted from the raw data to yield the net coincidence rate R_c. Note that the detector dark counts were also subtracted to obtain the net singles rate R_s and R_i. According to the theory of waveguide SPDC and assuming a perfect correlation between the signal and idler photons, we expect that R_s, R_i and R_c increase linearly with P_p. In Fig. 4.5, we fitted the experimental data with straight lines. It is seen that, at low pump powers, the singles rate indeed has a linear power dependence. However, at higher pump powers of $P_p \geq 1$ mW, the measured data deviate from the linear fit, resulting in a noticeable undercount in singles rates. We suggest that this kind of undercount is due to the fact that there were more than one downconverted pair present within the 20-ns gating period, thus causing the detectors to saturate. Therefore, we characterize the flux of our waveguide using only the data in the shaded region in Fig. 4.5, within which the singles rates and pump power levels were too low to cause detector saturation. The pair generation rate can be calculated according to,

$$R_{gen} = R_c/\eta_s\eta_i P_p \tag{4.6}$$

and we obtain a pair generation rate of $\sim 2.0 \times 10^7$ pairs/s/mW of pump. The result is in excellent agreement with our theoretical estimate of $\sim 2.1 \times 10^7$ pairs/s/mW. Note that the theoretical and measured generation rates are total-flux values because we used a 10-nm filter bandwidth that was much larger than the expected phase-matching bandwidth of 1.1 nm.

Excluding the dark counts of the detectors, the expected singles rates can be obtained from the net coincidence rate according to,

$$\tilde{R}_{s,i} = R_c/\eta_{i,s}\,, \tag{4.7}$$

We find $\tilde{R}_{s,i}$ is smaller than the measured rates because the measured singles included background photons that were primarily fluorescence photons. Hence the number of fluorescence photons are $(R_{s,i} - \tilde{R}_{s,i})$ per second, which can be compared with the true singles rates $\tilde{R}_{s,i}$. Over the 10-nm measurement bandwidth, which invariably included background photons outside of the phase-matching bandwidth, we found

that the ratio of total fluorescence photons to the total downconverted photons was $15 \pm 5\%$. This ratio was the averaged value for pump powers ranged from 37 μW to 0.3 mW.

4.3 Spectrum Characterization With Narrowband Filtering

The flux characterization using broadband filtering did not reveal any information about the spectrum of the downconverted photon. To characterize the SPDC spectrum, we used a tunable narrowband filter which has a polarization-independent Gaussian transmission spectral FWHM bandwidth of 0.79 nm, and a 50% peak transmission efficiency. The center wavelength of the filter can be tuned with a spectral resolution of 0.2 nm. The experimental setup in Fig. 4.4 was used with almost no change, except that the fiber-coupled filter was connected to the waveguide output PMF and was collimated for free-space output. We scanned the filter center wavelength from 1313.0 nm to 1319.0 nm, and recorded the corresponding singles counts in both signal and idler channels. A typical spectral histogram for signal photons is shown in Fig. 4.6, in which the dark counts of the detector was subtracted. Note that the histogram shown is not the true signal photon spectrum, due to the finite bandwidth of the narrowband filter. The measured data needs deconvolution to remove the effect of the filter transmission bandwidth. Although a direct deconvolution technique can be used, it was not pursued in this case. The measured spectrum showed some irregular features compared to a smooth sinc-squared shape. Therefore the most efficient way to extract the true spectrum was to fit the measurement result using an ideal sinc-squared function, while we keep the peak magnitude, bandwidth and a constant background as free parameters for fitting. The solid theory curve corresponding to the fit is also shown in Fig. 4.6 too. After fitting, we obtain an effective signal-photon bandwidth of ~ 1.29 nm, which compares favorably with the theoretical predication of 1.1 nm by Eq. (2.20). In our narrowband measurement we

observed a pedestal in the spectrum near 1313.5 nm. A similar feature has also been reported in a waveguide SPDC spectrum elsewhere [26]. Furthermore, a comparable satellite peak centered at 1318.5 nm was also observed in the idler output spectrum (not shown here). The satellite peaks, located 2.5 nm from the peak wavelength, may be caused by nonuniformity in the periodic grating structure throughout the length of the crystal. According to [45], a systematic error in the duty cycle of the periodic grating in a crystal would cause secondary peaks in the SPDC spectrum. In addition, a local non-inhomogeneity of the grating would also result in an imperfect sinc-sqaured spectral shape. This is because the SPDC efficiency is no longer uniform throughout the length of the crystal, but only a uniform efficiency generates a sinc-function in spectral domain. Such local non-inhomogeneity has been observed in bulk PPKTP crystals [50]. Lastly, the satellite peaks could also be a result of higher-order SPDC that we discussed in detail in chapter 3. The multi-mode processes $11 \longrightarrow 01+10$ and $02 \longrightarrow 30+00$ might have contributed to the side spectral pedestals, but we cannot confirm this postulation at this time.

In Fig. 4.6 there is a uniform band of background counts of $\sim$10 counts per 0.25 nm bin. We attribute this background to fluorescence photons. The pump-induced fluorescence was not a phase matched process, so spectrally they extended over a bandwidth that is much larger than the bandwidth of interest, as suggested in Fig. 4.6. At the spectral peak in Fig. 4.6, the ratio of fluorescence photons polarized along the Y crystal axis to the downconverted signal photons is $\sim$10%. A similar measurement for the other polarization and the idler photons shows a slightly lower value. However, if we integrate the background counts over a bandwidth of 10 nm we obtain a ratio that is higher than the 15% we measured using only the 10-nm filter. This apparent discrepancy resulted from our arrangement of the filters. In this case, the narrowband fiber filter was connected directly to the waveguide output fiber, thus the strong residual pump produced additional background photons within the narrowband filter. We confirmed this phenomenon by directly coupling the pump visible laser light into the narrowband filter. We detected noise photons at 1316 nm band. Adding the narrowband filter immediately after the 10-nm pump-blocking filter would have

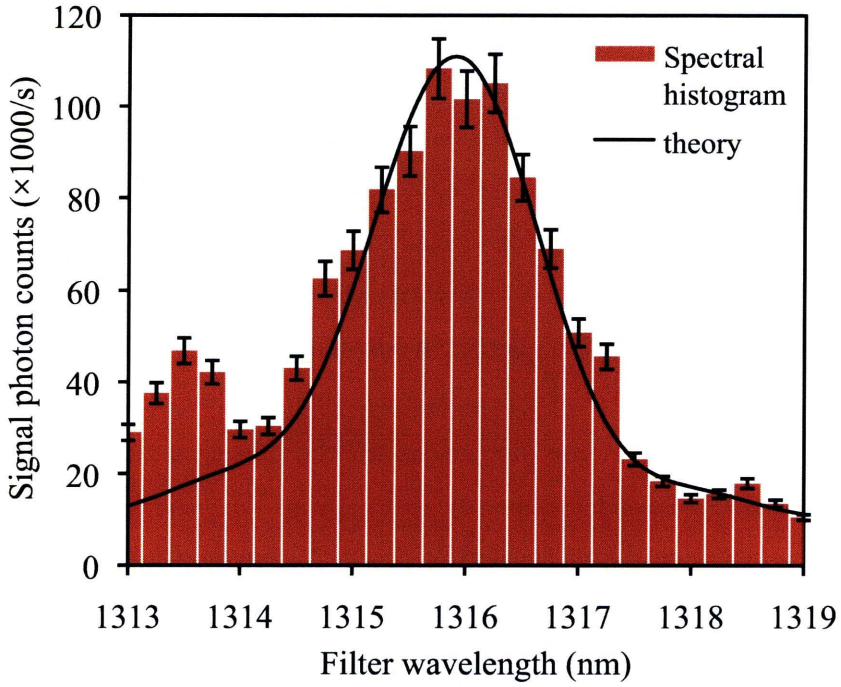

Figure 4-6: Spectral histogram of light polarized along the Y crystal axis including signal photons and fluorescence photons. The theoretical curve is obtained by a convolution of the Gaussian transmission spectrum of the filter and a sinc-squared phase-matching function. Bin-width is 0.25 nm.

taken care of the problem. This seemingly simple step was not taken because the narrowband filter was fiber-coupled whereas the long-pass filter was a bulk glass filter.

To accurately measure the amount of fluorescence photons, we placed the narrowband filter behind the pump-blocking long-pass filter and immediately in front of the detectors. By fixing the narrowband filter center wavelength at 1316 nm, we changed the waveguide temperature, therefore the signal spectrum was shifted to longer wavelengths and the idler spectrum was shifted towards shorter wavelengths. The measured singles counts versus the detuned wavelength of the spectral peak with respect to 1316 nm is plotted in Fig. 4.7. To suppress the downconverted photons and measure only the fluorescence photons, it is necessary to detune the signal and

idler spectra by >6 nm such that they were completely outside the bandwidth of the narrowband filter. We observed that the ratio of Y polarized fluorescence photons to signal photons within the phase-matching bandwidth was ~2.4%, while the ratio of Z polarized fluorescence photons to idler photons within the phase-matching bandwidth was ~1.7%. Overall the true ratio of the total fluorescence to the total downconverted photons is $\sim$ 2% for our waveguide source. This value seems to be consistent with the previously obtained ratio of $15 \pm 5\%$ over the entire 10 nm bandwidth. We note that the amount of fluorescence photons in our source is consistently lower than those reported in previous PPKTP waveguides that were pumped at shorter wavelengths [22, 24, 26, 51]. Lastly, we also plot in Fig. 4.7 the sinc-squared spectra convoluted with the bandpass filter, the same way as we did in Fig. 4.6. For both signal and idler spectra, we saw a bump located at about 2.5 nm from the spectral peak, at which the measured count significantly exceeded the theoretical prediction shown as a solid curve. These observed bumps are consistent with the satellite peaks found in Fig. 4.6. The cause of such bumps are being investigated at this time.

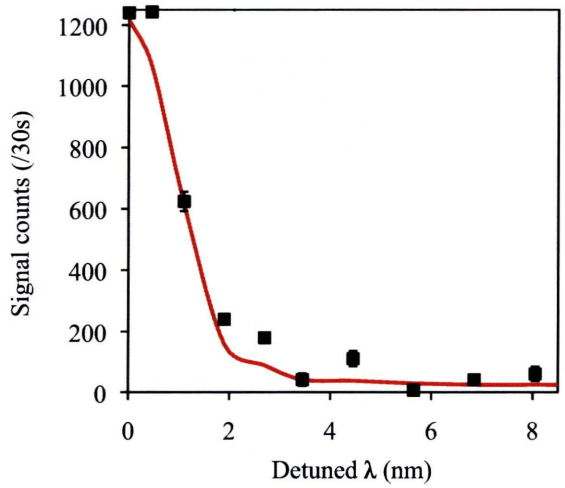

(a)

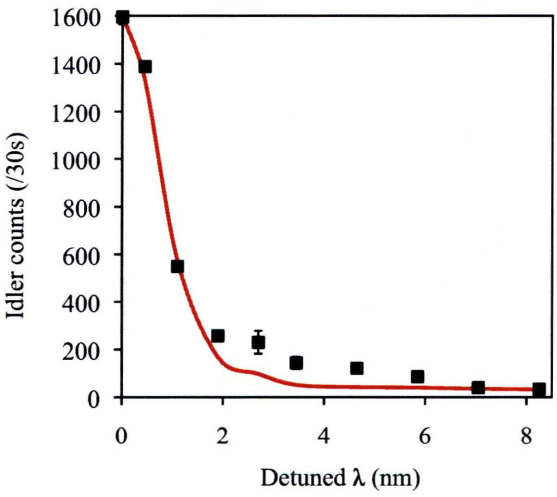

(b)

Figure 4-7: Singles counts (dark count subtracted) under temperature detuning. (a) Signal (along Y crystal axis) counts versus the detuned wavelengths. (b) Idler (along Z crystal axis) counts versus the detuned wavelengths.

Chapter 5

HOM Interference Measurement

5.1 Introduction

The Hong-Ou-Mandel (HOM) interference is a two-photon interference effect that was demonstrated experimentally by Hong, Ou, and Mandel [33] in 1987. It occurs when two identical photons, one photon per input, enter a 50-50 beam splitter. When the temporal overlap of the photons at the beam splitter is perfect, the two photons will always exit together in the same output port. If there are two photodetectors monitoring the output modes of the beam splitter, the coincidence rate of the detectors will drop to zero when the identical input photons overlap perfectly in time. This is called the HOM dip. The minimum drops to zero when the two photons are perfectly identical in all properties.

The distinctive feature of HOM dip makes it a powerful tool for measuring the distinguishability between two photons generated in a photo-pair source. Since indistinguishability is essential for polarization entanglement and virtually all kinds of quantum interference between photons, obtaining a high HOM interference visibility is the pre-requisite for generating high quality polarization-entangled photons. HOM measurements on currently developed waveguide photon-pair sources have failed to show high visibility, as compared with the high visibility ($\geq 95\%$) observed in bulk-crystal sources [32]. As a consequence, no high-quality polarization entangled photons have been efficiently generated in a waveguide. The most recent result measured on

a PPLN waveguide showed a ~85% HOM visibility at 1.3 μm [27]. Note that this reported HOM visibility was defined as $V = 1 - C_{min}/C_{max}$, where $C_{\max}$ and $C_{\min}$ are the maximum and minimum coincidence counts with accidentals subtracted, respectively. To be consistent with the standard definition of classical interference as well as the definition of quantum interference visibility for polarization entanglement, we suggest that we use the following definition of HOM visibility throughout this thesis,

$$V_{\mathrm{HOM}} = \frac{C_{max} - C_{min}}{C_{max} + C_{min}}. \tag{5.1}$$

The reasons for the low HOM visibility in previous waveguide sources are still unclear. From the theory of waveguide SPDC, we know that the spectrum of the down-converted photons should be the same as the single-spatial-mode output in bulk crystals. Namely, the signal and idler photons should have identical spectra with a sinc-squared shape. From our previous spectrum characterization in chapter 4, we have learned that the waveguide output spectrum was fairly consistent with the theoretical prediction, except for those satellite peaks observed adjacent to the main spectral peak. Such asymmetric spectral structure indicates that the spectral overlap between the signal and idler photons over a large bandwidth degraded, because the signal spectrum is the "mirror image" of the idler spectrum due to frequency anti-correlation. Therefore, to achieve a high degree of indistinguishability between signal and idler photons, we should use a narrowband filter whose bandwidth is equal or smaller than the phase-matching bandwidth of SPDC to remove the asymmetric features in the two-photon spectrum. In Sect. 5.4, we will examine the effect of a larger measurement bandwidth on the HOM visibility.

In our fiber-coupled source, the signal and idler photons were single-mode fiber coupled, and therefore were automatically in the same spatial mode. Hence, by using a fiber 50-50 beam splitter, any spatial mode distinguishability between the two photons was avoided. In this work, we setup the HOM experiment using both a narrowband filter and a fiber 50-50 coupler. We expect the signal and idler photons to be highly indistinguishable in all degrees of freedom, and a high HOM visibility

should be obtained.

Our continuous-wave waveguide source is also subject to multi-pair generation. Namely, when n (> 1) pairs are generated within a coincidence time window, there is a possibility that uncorrelated photons from different pairs are detected, producing a false coincidence count. Note that this kind of false coincidences caused by multi-pair generation is different from accidental coincidences. The latter can be easily measured by delaying the detection in one channel, and recording the coincidence counts due to independent events. However, the multi-pair induced coincidences cannot be identified using a similar method, at least not with photon number non-resolving detectors. It was shown in the literature that such multi-pair generation event could degrade the quantum interference visibility of two polarization entangled photons as the pair flux increases. We expect the same visibility degradation to occur for HOM measurement. In this chapter, we investigate the effect of multi-pair generations on HOM visibility, and derive a simple expression at the low pump power regime. The expression we obtain is important, because it allows us to run the HOM experiment with the correct operating condition to achieve a high visibility.

Another feature of HOM measurements is that the width of the HOM dip is related to the two-photon coherence time, which in turn gives the two-photon spectral bandwidth. This effect can be understood in a similar manner to autocorrelation measurement in ultra-fast optics. Only when two photons are overlapped in time, there could be a drop in the coincidence count at the outputs of a 50-50 coupler. Therefore, HOM interference can be used to accurately measure the temporal width and the spectral width of the signal and idler photons. We note that this method gives a more accurate result than the spectral histogram method we used in chapter 4. In the latter case, we could not discern the coherent spectrum of a single photon from the background photons, which results in a measured single photon bandwidth that is slightly larger than the actual bandwidth. However, using HOM interference, the incoherent background photons do not contribute to the HOM dip, and what we measure can only be the two-photon coherence bandwidth. In the last section of this chapter, we use this method to characterize the two-photon bandwidth of our

waveguide output, which should be compared to the theory we developed earlier in chapter 2.

5.2 Experimental Setup and Measurement Result

One of the simplest ways to generate polarization-entangled photons is to send a pair of orthogonally polarized photons as two inputs to a 50-50 beam splitter [32], which requires that the two photons be completely indistinguishable in their spatial, spectral, and temporal characteristics. The HOM setup shown in Fig. 5.1 is ideal for measuring the distinguishability of two individual photons. We used the tunable narrowband filter to remove the satellite peaks from the output spectra. The filtering also provided a detection bandwidth that was slightly smaller than the phase-matching bandwidth and ensured a high degree of signal-idler spectral overlap. For maximum spectral overlap between signal and idler we repetitively scanned the signal and idler spectra while we fine-tuned the waveguide temperature. At a pump wavelength $\lambda_p = 658.0$ nm, we found the signal and idler outputs were wavelength degenerate at a temperature of 19.5° C. Additional free-space filtering of the residual pump and fluorescence photons were provided by the long-pass filter and the 10-nm band-pass filter.

After the signal and idler photons were separated by a PBS, we sent the horizontally polarized signal through a prism delay stage that was controlled by a motorized translation stage. We also made sure that the overall transmission of the signal arm was minimally perturbed over the entire scanning range of the motorized stage. The signal was then coupled into one of the input ports of a 50-50 fiber coupler. We coupled the vertically polarized idler into the other port of the 50-50 fiber coupler and we used a paddle polarization controller to match the polarization of the idler to that of the signal. To ensure a completely identical polarization state for both photons, we measured the classical interference of our interferometer by using a fiber-coupled diode laser at 1316 nm. The classical interference visibility was measured at $\sim 99.9\%$ after we adjusted the paddle polarization controller. We noted that the optimal po-

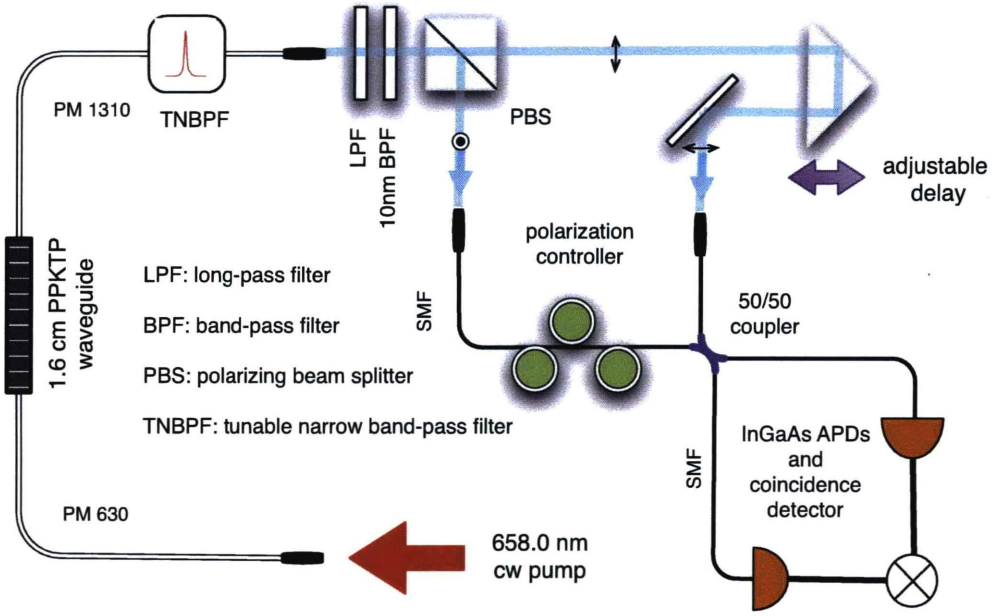

Figure 5-1: Experimental setup of HOM quantum interference measurement.

larization states of the photons were stable for a few hours, which was longer than our measurement time. This means that the polarization indistinguishability was ensured during the measurements. The total path lengths of the fiber and free space were carefully matched for the two arms. The outputs of the 50-50 fiber beam splitter were sent to InGaAs single-photon counters for coincidence measurements, as described in chapter 4. We note that the splitting ratio of the fiber beam splitter was 49:51, which had the effect of reducing the HOM visibility by 0.2% according to Eq. (11) in [33].

Fig. 5.2 shows the HOM measurement results at a pump power $P_p = 57\mu$W, in which the raw coincidence counts (solid blue diamonds) and the separately measured accidental coincidences (open red squares) are plotted as a function of the path length difference between the two arms. After subtracting the accidental coincidences from the raw data in Fig. 5.2, we obtain a HOM quantum-interference visibility $V = (C_{\max} - C_{\min})/(C_{\max} + C_{\min}) = 98.2 \pm 1.0\%$, , respectively. To our knowledge, this is the highest HOM visibility ever reported for waveguide-based photon-pair sources. The 1% uncertainty of the measured visibility is mainly due to the uncertainty of

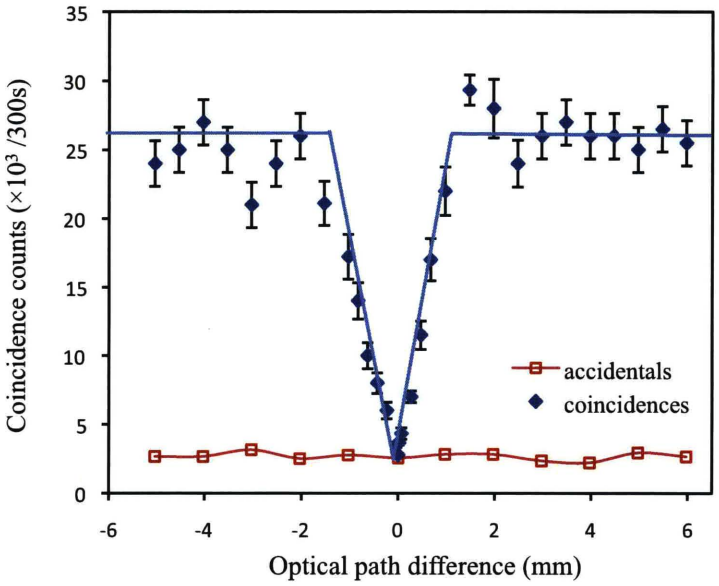

Figure 5-2: Measured HOM coincidences and accidentals counts in 300s as function of the optical path difference between the signal and idler arms at waveguide temperature of 19.5 °C and with 57 μW pump power. HOM quantum interference visibility is 98.2% with accidentals subtracted from the raw data.

the accidental coincidence rates caused by the high dark count rates of our InGaAs detectors as described in chapter 4. To achieve a satisfactory photon statistics, we used a 300s measurement time per sample, and each data was obtained by averaging over 20 samples. As a result, our experiment took a long acquisition time. We suggest that the acquisition time could be shortened significantly by using a superconducting nanowire single photon detector (SNSPD) operated in a free-running mode. In addition, the known low dark count rates of SNSPDs could improve the accuracy of HOM measurements, because the accidental coincidence will be much lower than measured using our InGaAs APDs. The base-to-base width of the HOM dip is 2.3 ± 0.13 mm, corresponding to a two-photon coherence time of $\tau_c = 3.83 \pm 0.21$ ps. Equivalently we calculated a two-photon bandwidth of 0.76 ± 0.04 nm from the two-photon coherence time according to Eq. (5.2). The result is consistent with the narrowband filter bandwidth of 0.79 nm. Here the two-photon bandwidth is defined as the half zero-to-zero

width of the sinc-squared phase-matching function.

$$\delta\lambda_c = \frac{\lambda^2}{2c\tau_c} \tag{5.2}$$

The high HOM visibility was a result of our use of a single-mode fiber beam splitter to ensure spatial mode overlap and our careful adjustment of the waveguide temperature and the use of a narrowband filter to optimize the spectral overlap. The result shows that the photon-pairs generated from our waveguide are indeed highly indistinguishable, therefore they are suitable for generating high quality polarization entanglement.

5.3 Effect of Multi-Pair Generation

Taking into account the imperfect polarization overlap and the non-ideal 50-50 splitting of the fiber coupler, we should have obtained an even higher HOM visibility of $\sim 99.7\%$. We believe that the visibility did not reach even higher because of multi-pair generation in the downconversion process. For a highly efficient SPDC waveguide source, the probability of double-pair generation within a coincidence window is not negligible even at a low pump power level. In this section, we develop a simple Poisson model to quantify the effect of multiple pair generation on HOM interference measurement for our waveguide setup in Fig. 5.1. The theoretical predictions using this model are then compared with the experimental result at various pump powers.

Continuous-wave SPDC output is multi-temporal mode because the coincidence measurement time window of 2.5 ns is large compared with the temporal width 3.83 ps of the output photon wave packet. Here we exclude the small amount of the fluorescence photons, since their contribution to the total coincidence could be subtracted as accidental coincidences. Therefore, the pair generation probability within a coincidence time window follows the Poisson statistics, with a mean pair generation number α.

$$p_n(\alpha) = \frac{e^{-\alpha}\alpha^n}{n!}, \sum_{n=0}^{\infty} p_n(\alpha) = 1 \tag{5.3}$$

where $p_n(\alpha)$ is the probability for exactly n pairs occurring in a coincidence window. To calculate the HOM visibility including the multi-pair generation effects, we only need to determine the probabilities associated with the maximum and minimum coincidence C_{max} and C_{min}, respectively. In a HOM measurement, C_{min} is measured at the HOM dip, where signal and idler photons are supposed to overlap completely in time. On the other hand, C_{max} is measured at sufficiently long time delays between the two photons so that the signal and idler photons are completely distinguishable. The minimum and maximum coincidence probabilities are then given by,

$$C_{min} = \sum_{n=1}^{\infty} p_n(\alpha) c_{min}(n), \tag{5.4}$$

$$C_{max} = \sum_{n=1}^{\infty} p_n(\alpha) c_{max}(n), \tag{5.5}$$

where $c_{min}(n)$ and $c_{max}(n)$ are the coincidence probabilities for an output of exactly n independent pairs of photons in multi-temporal modes. Note that the summation starts from $n = 1$ because $c_{min}(0) = c_{max}(0) = 0$. For $c_{max}(n)$, there are $2n$ independent photons, each of them will exit either of the two output modes of the 50-50 coupler in a completely random fashion. An example scenario of n pair of photon transmission through the coupler is shown in Fig. 5.3. Among $2n$ photons, k of them may exit output 1 and go to detector 1, and the remaining $2n - k$ photons go to detector 2. This specific arrangement happens with a probability of $\binom{2n}{k}/2^{2n}$ with the binomial coefficient

$$\binom{2n}{k} = \frac{(2n)!}{(2n-k)!k!} \tag{5.6}$$

for $0 \leq k \leq 2n$. For a given arrangement, one requires at least one detection event at the detector 1 and at least one detection event at detector 2 to yield a coincidence count for $c_{max}(n)$. Here we assume the detectors are not photon number-resolving. For the case of $c_{min}(n)$, each pair of photons are perfectly overlapped in time so they will exit either output together with a probability of 1/2. From a coincidence point

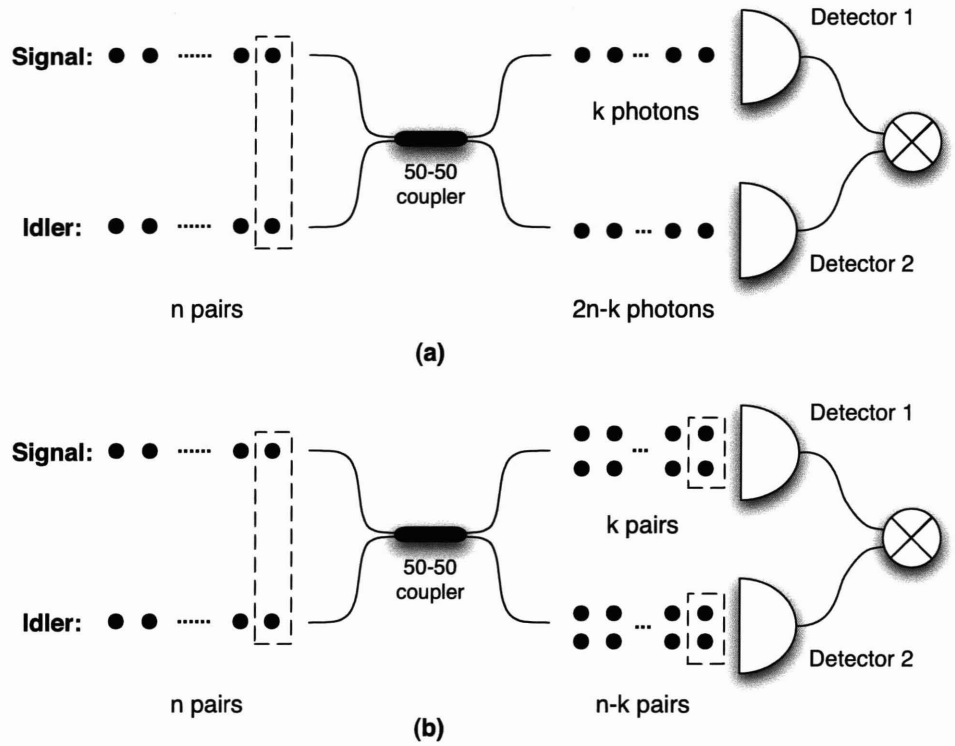

Figure 5-3: Example transmission and detection of multi-pair photon generated within a coincidence window. (a) a scenario for $c_{max}(n)$ in which signal and idler photons of each photon pair do not overlap in time. (b) a scenario for $c_{min}(n)$ in which signal and idler photons of each photon pair completely overlap in time.

of view, each pair acts like a single photon. Therefore, in a scenario that k pairs of photons go to detector 1, and the remaining $n-k$ pairs of photons go to detector 2, the probability for this to happen is $\binom{n}{k}/2^n$. To yield a coincidence count, at least one of the $2k$ photons should be detected by detector 1, and at least one photon should be detected at detector 2. Assuming that both the signal and idler paths have a system detection efficiency η, we can express the maximum and minimum coincidence probabilities according to the above argument,

$$c_{max}(n) = \frac{1}{2^{2n}} \sum_{k=0}^{2n} \binom{2n}{k} [1-(1-\eta)^k][1-(1-\eta)^{2n-k}], \tag{5.7}$$

$$c_{min}(n) = \frac{1}{2^n} \sum_{k=0}^{n} \binom{n}{k} [1-(1-\eta)^{2k}][1-(1-\eta)^{2(n-k)}]. \tag{5.8}$$

Using the expressions of Eq. (5.3-5.8), it is straightforward to compute the minimum and maximum coincidence probabilities, and obtain the HOM visibility as a function of the mean pair generation number α. For practical considerations, we are interested in the multi-pair effect for small α in which case the terms with more than two pairs can be ignored. The Poisson distribution coefficients then become $p_1(\alpha) = \alpha e^{-\alpha}$ and $p_2(\alpha) = (\alpha^2/2)e^{-\alpha}$. And one easily finds,

$$C_{max}(n) = \frac{1}{2}\alpha e^{-\alpha}\eta^2[1 + 3\alpha(1 - \eta + \frac{7}{24}\eta^2)] \tag{5.9}$$

$$C_{min}(n) = \alpha^2 e^{-\alpha}\eta^2(1 - \frac{\eta}{2})^2 \tag{5.10}$$

and the corresponding HOM visibility to the first order of α and η is

$$V_{\text{HOM}} = 1 - 4\alpha(1 - \eta). \tag{5.11}$$

Note that for a low system detection efficiency $\eta \sim 1.1\%$, V_{HOM} has little dependence on the system loss, and is dominantly determined by the pumping level. In particular, low coincidence detection rates do not imply low pair generation rates. This is especially true for a high flux waveguide photon pair source. When pumped at 1 mW, our waveguide produced 2×10^7 pairs/s, which corresponded to $\alpha = 5\%$. The measured HOM visibility would be only $\sim 80\%$, as predicted by Eq. (5.11). Experimentally, we verify the relationship of Eq. (5.11) by repeating the HOM interference measurements at various pump powers. Fig. 5.4 plots the measured HOM visibility (with accidentals subtracted) as a function of the mean pair number. As α increased from 0.3% to 4.0%, the HOM visibility dropped from 98.2% to 85.5%. The experimental result is in good agreement with the theoretical prediction of Eq. (5.11) (solid line) that includes the effect of double-pair generation. We notice that for $\alpha > 4\%$, the experiment data starts to curve up. This deviation from the linear relationship is due to our first order approximation for very small α. To better describe the effect of multi-pair generation on HOM visibility for $\alpha > 4\%$, we could include the 3-pair contributions, eg. $c_{max}(3)$ and $c_{min}(3)$, and compute V_{HOM} to the second order of α.

In this case, we also include $p_3(\alpha) \approx (\alpha^3/6)e^{-\alpha}$, and we find,

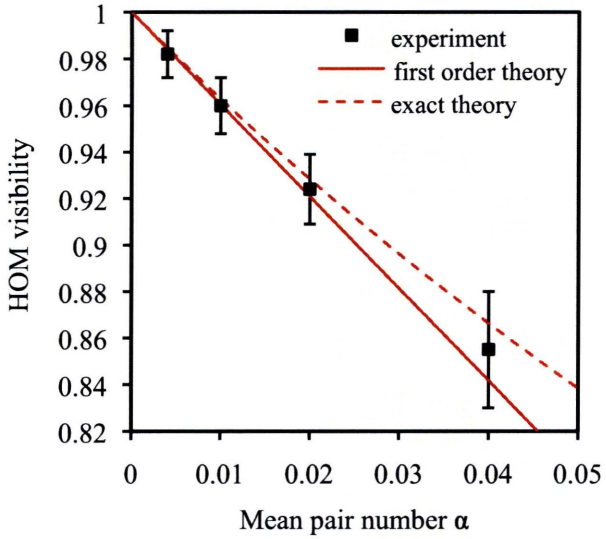

Figure 5-4: Experimental HOM quantum interference visibilities versus the mean pair number within a coincidence window of 2.5 ns. The solid theoretical curve takes into account only double-pair generation according to Eq. (5.11). The theory curve assumes a perfect spectral overlap between the signal and idler photons.

$$V_{\mathrm{HOM}} = 1 - 4\alpha(1-\eta) + 16\alpha^2(1-2\eta). \tag{5.12}$$

In Fig. 5.4, we plot the expected HOM visibility (dashed curve) if we include contributions from all multi-pair events. We note that as α increases, the experimental data drifts away from the straight line of Eq. (5.11) towards the more exact theoretical prediction.

More importantly, Eq. (5.11) reveals a possible source of experimental challenge in obtaining a high HOM visibility from a waveguide photon pair source. HOM visibility can be easily compromised when one fails to pump the waveguide at a very low power. Note that for quantum interference between a pair of polarization entangled photons, it was found that the visibility $V_{\mathrm{pol.entangle}} = 1 - \alpha$ for small α. Thus the HOM visibility is more prone to the adverse effect of multi-pair generations. Intuitively, this

is because when analyzing the polarization entangled photons, our choice of measuring photons at two specific polarization states provide a better discrimination against the multi-pair generation events. Whereas in a HOM measurement, all photons are in the same polarization state, thus multi-pair generation events cannot be discriminated at all. For an ultra-high brightness waveguide photon pair source, one often tends to operate it at high flux. This could often be the case when the output is in telecom wavelengths in which efficient detectors are not available. However, Eq. (5.11) shows a fundamental trade-off between the brightness and the quantum interference visibility of a photon-pair source. To generate and detect highly indistinguishable photons, it is necessary to operate the source at a very low pumping. In this sense, having high brightness alone might not be always good for a source. Instead, source brightness and high HOM interference visibility should be considered together as performance metrics for evaluating the quality of a photon pair source. Moreover, knowing the trade-off allows the waveguide SPDC source to be operated according to the needs of specific applications. In the present case, with single spatial-mode operation and low pumping levels, we have achieved in our waveguide a HOM quantum-interference visibility that is significantly higher than previous high-brightness waveguide sources [26, 27].

5.4 HOM Interference Measurement without Narrowband Filtering

So far, we have been focused on obtaining high HOM visibility from the waveguide source. HOM interference could also be used to characterize the spectral overlap between the signal and idler photons. With the narrowband filter removed, two broadband photons could interference at the 50-50 beam splitter. If the spectra of the two photons are perfectly overlapped, high HOM visibility should still be obtained. However, if there is any asymmetric feature present in the two photon spectra, HOM dip will not be zero, and the the amount of imperfect spectral overlap will manifest

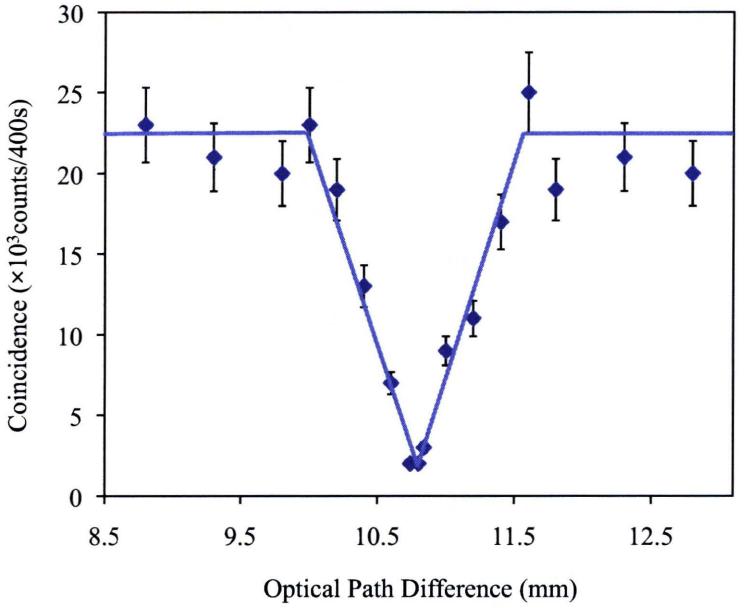

Figure 5-5: Measured HOM coincidence counts in 400s as function of the optical path difference between the signal and idler arms at waveguide temperature of 19.5 °C and with 57 μW pump power. HOM quantum interference visibility is 84.2% with accidentals subtracted from the raw data.

as degraded HOM visibility. Therefore, broadband HOM measurement offers a way to test the genuine spectral indistinguishability of photon pairs generated from a waveguide. Additionally, this experiment can also measure the two-photon bandwidth in resemblance to the autocorrelation measurement of ultrashort optical pulses. As the temporal overlap between the two photon wave packet is varied by delaying one signal with respect to the other, the coincidence count will exhibit a HOM dip whose width is related to the temporal bandwidth of the single photon wave packet. Let the base-to-base width of the HOM dip be l_c, the two-photon coherence time is then $\tau_c = l_c/2c$. The two-photon bandwidth, which is defined as half the zero-to-zero phase-matching bandwidth of the sinc-squared function, is related to the two-photon coherence time by Eq. (5.2).

For measuring the two-photon bandwidth, we performed a HOM measurement without the 0.79-nm narrowband filter. For a detection bandwidth much larger than

the phase-matching bandwidth, any asymmetric feature in the signal and idler spectra such as the satellite peak in Fig. 4-6 would cause the HOM visibility to degrade, because the signal and idler photons were no longer completely indistinguishable. Nevertheless, the temporal and spectral bandwidth of the two-photon state can still be accurately determined. Under the same operating conditions with a pump power of 57 μW, we scanned the optical path difference between the signal and idler photons. Since the removal of the PM fiber narrowband filter changed the path lengths of two photons, the displacement of the delay stage where HOM dip occurred was also changed. Fig. 5-5 plots the HOM coincidence counts against the displacement of the delay stage. An HOM dip was clearly seen, and the HOM visibility of $V_{\text{broadband}} = 84.2\%$ was obtained after subtraction of accidental coincidence count. The observed base-to-base width of the HOM dip of 1.6 mm yields a two-photon coherence time of 2.67 ps, or a two-photon bandwidth of 1.08 nm according to Eq. (5.2). This measured two-photon bandwidth is in excellent agreement with the phase-matching bandwidth calculated from Eq. (2.20) in chapter 2.

Assuming the difference between the broadband and narrowband visibilities was due to spectral indistinguishability, we estimate that the spectral overlap between signal and idler photons was $\sim 92\%$ without the narrowband filter. To further verify our speculation, we measured broadband HOM visibilities at different pump powers. Similar to the multi-pair generation effect discussed earlier, at high pump powers, the HOM visibility is expected to degrade. However in the broadband case, we have to modify the calculations for $c_{min}(n)$, because even when the two photons are temporally overlapped, they are not completely overlapped spectrally. We define the two-photon spectral overlap as γ, so any pair of photons will exhibit the HOM interference effect with a probability of only γ, and the pair will behave like two independent photons with a probability of $1 - \gamma$. The experimental result is plotted in Fig. 5-6. The theoretical curve is calculated based on the multi-pair effect result with a modification to include the imperfect spectral overlap between the two photons of 92%. We see that the measurement data is in good agreement with the theoretical prediction, which confirms our assumption of $\sim$92% spectral overlap. Furthermore,

it is seen that in the broadband case, the HOM visibility degrades even more quickly as the pump power increases, as compared with the case for narrowband HOM. The broadband HOM could drop to below 50% at a moderate pump power.

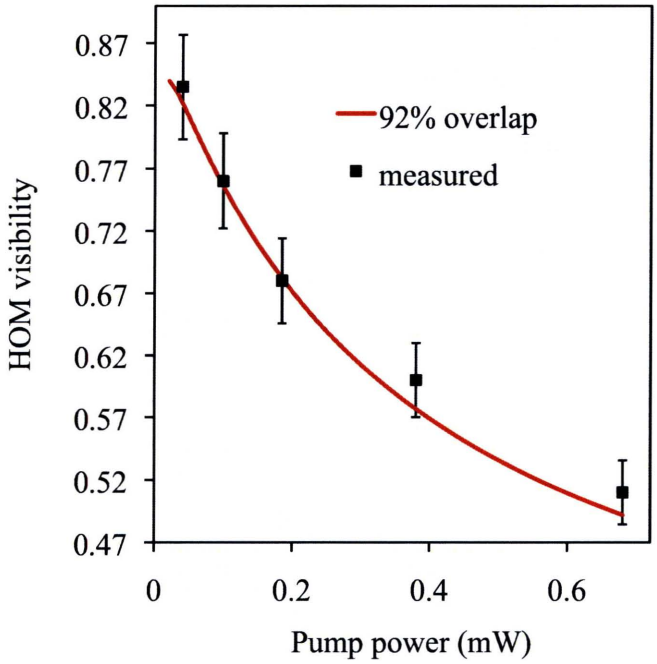

Figure 5-6: Experimental HOM quantum interference visibilities versus the pump power. The solid theoretical curve takes into account the double-pair generation. The theory curve assumes a 92% spectral overlap between the signal and idler photons.

The 92% spectral overlap between the signal and idler photons without narrowband filtering is an encouraging result. It confirms that the narrowband outputs of our waveguide source are spectrally highly indistinguishable. The imperfect overlap are mainly caused by the asymmetric side-peaks in the signal or idler photon spectrum. Such side-peaks can be easily removed by narrowband filtering, as we did in the narrowband HOM experiment. Overall, the photon pair output of our waveguide are well suited for generating polarization entangled photons. Considering its high brightness, waveguide photon pair sources might outperform bulk crystal sources for the application of entanglement generation.

Chapter 6

Conclusions

In this work, we have experimentally demonstrated the production of narrowband correlated photon pairs at 1316 nm using a fiber-coupled type-II phase-matched PPKTP waveguide, yielding a source brightness of 2.0×10^7 pairs/s/mW of pump over the measured phase-matching bandwidth of 1.08 nm. The output flux of our waveguide source was measured to show excellent agreement with a new theoretical model of SPDC in a nonlinear waveguide. The model considers the transverse index profile of a nonlinear crystal waveguide that imposes an effective transverse momentum on the phase-matching conditions. We find that the effective grating leads to a broader transverse bandwidth of the signal and idler outputs, which in turn explains the much higher spectral brightness of a waveguide SPDC source compared with a bulk-crystal SPDC source.

Our PPKTP waveguide source is particularly useful for applications in the important telecommunication band. The source was fabricated with single-mode fiber coupling at both the input and output ends to facilitate connection to a standard fiber-optic network. We have measured a ratio of fluorescence photons to downconverted photons of 1:50 for our waveguide source, which is much lower than those observed in previous waveguide sources and is comparable to or better than that of a bulk-crystal source. Furthermore, at a low pump power, our device achieved a HOM quantum-interference visibility of 98.2%, the best ever reported for a waveguide SPDC source. This waveguide SPDC source is well suited for generation of high-quality en-

tangled photons for fiber-optic applications in quantum information science such as quantum key distribution and entanglement distribution. The possibility of an integrated waveguide device incorporating a SPDC sources, modulators, and directional couplers may lead to simpler and more efficient development in future long distance quantum communication protocols.

Bibliography

[1] C. Bennett and G. Brassard, "Quantum cryptography: Public key distribution and coin tossing," in Proc. IEEE Int. Conf. on Computers, Systems, and Signal Processing, Bangalore, India, 175 IEEE, New York (1984).

[2] A. Ekert, "Quantum cryptography based on Bell's theorem," Phys. Rev. Lett. **67,** 661 (1991).

[3] P. W. Shor, "Polynomial-time algorithms for prime factorization and discrete logarithms on a quantum computer," SIAM J. Computing **26,** 1484 (1997).

[4] L. Grover, "A fast quantum mechanical algorithm for database search," in Proceedings of 28th Annual ACM Symposium on the Theory of Computing (STOC) 212219, ACM Press, New York (1996).

[5] C. M. Caves, "Quantum-mechanical noise in an interferometer," Phys. Rev. D **23,** 1693-1708 (1981).

[6] V. Giovannetti, S. Lloyd, and L. Maccone, "Quantum-Enhanced Measurements: Beating the Standard Quantum Limit," Science **306,** 1330-1336 (2004).

[7] J. T. Barreiro, N. K. Langford, N. A. Peters, and P. G. Kwiat, "Generation of hyperentangled photon pairs," Phys. Rev. Lett. **95,** 260501 (2005).

[8] J. T. Barreiro, T.-C. Wei, and P. G. Kwiat, "Beating the channel capacity limit for linear photonic superdense coding," Nat. Phys. **4,** 282-286 (2008).

[9] I. Marcikic, H. de Riedmatten, W. Tittel, H. Zbinden, M. Legré, and N. Gisin, "Distribution of time-bin entangled qubits over 50 km of optical fiber," Phys. Rev. Lett. **93,** 180502 (2004).

[10] T. Kim, I. Stork genannt Wersborg, F. N. C. Wong, and J. H. Shapiro, "Complete physical simulation of the entangling-probe attack on the Bennett-Brassard 1984 protocol," Phys. Rev. A **75,** 042327 (2007).

[11] C. Santori, D. Fattal, J. Vučković, G. S. Solomon, and Y. Yamamoto, "Indistinguishable photons from a single-photon device," Nature **419,** 594-597 (2002).

[12] X. Li, P. L. Voss, J. E. Sharping, and P. Kumar, "Optical-fiber source of polarization-entangled photons in the 1550 nm telecom band," Phys. Rev. Lett. **94,** 053601 (2005).

[13] J. Sharping, J. Chen, X. Li, P. Kumar, and R. Windeler, "Quantum-correlated twin photons from microstructure fiber," Opt. Express **12,** 3086-3094 (2004).

[14] J. Chen, J. Fan, M. D. Eisaman, and A. Migdall, "Generation of high-flux hyperentangled photon pairs using a microstructure-fiber Sagnac interferometer," Phys. Rev. A **77,** 053812, 2008.

[15] A. Zeilinger, "Long-distance quantum cryptography with entangled photons" in Quantum Communications Realized, ed. Y. Arakawa, H. Sasaki, H. Sotobayaski, Proc. SPIE V. 6780 (SPIE Bellingham WA, 2007), 6780-09.

[16] C. Kurtsiefer, P. Zarda, M. Halder, H. Weinfurter, P. M. Gorman, P. R. Tapster, and J. G. Rarity, "Quantum cryptography: A step towards global key distribution," Nature **419,** 450 (2002).

[17] T. Schmitt-Manderbach, H. Weier, M. Fürst, R. Ursin, F. Tiefenbacher, T. Scheidl, J. Perdigues, Z. Sodnik, C. Kurtsiefer, J. G. Rarity, A. Zeilinger, and H. Weinfurter, "Experimental demonstration of free-space decoy-state quantum key distribution over 144 km," Phys. Rev. Lett. **98,** 010504 (2007).

[18] D. Bouwmeester, J. W. Pan, K. Mattle, M. Eibl, H. Weinfurter, and A. Zeilinger, "Experimental quantum teleportation," Nature **390,** 575-579 (1997).

[19] Y. Tokunaga, S. Kuwashiro, T. Yamamoto, M. Koashi, and N. Imoto, "Generation of high-fidelity four-photon cluster state and quantum-domain demonstration of one-way quantum computing," Phys. Rev. Lett. **100,** 210501, 2008.

[20] R. Prevedel, P. Walther, F. Tiefenbacher, P. Böhi, R. Kaltenbaek, T. Jennewein, and A. Zeilinger, "High-speed linear optics quantum computing using active feed-forward," Nature **445,** 65-69 (2007).

[21] K. Chen, C.-M. Li, Q. Zhang, Y.-A. Chen, A. Goebel, S. Chen, A. Mair, and J.-W. Pan, "Experimental realization of one-way quantum computing with two photon four-qubit cluster states," Phys. Rev. Lett. **99,** 120503, 2007.

[22] K. Banaszek, A. B. U'Ren, and I. A. Walmsley, "Generation of correlated photons in controlled spatial modes by downconversion in nonlinear waveguides," Opt. Lett. **26,** 1367–1369 (2001).

[23] S. Tanzilli, H. de Riedmatten, W. Tittel, H. Zbinden, P. Baldi, M. de Micheli, D. B. Ostrowsky, and N. Gisin, "Highly efficient photon-pair source using periodically poled lithium niobate waveguide," Electron. Lett. **37,** 26–28 (2001).

[24] A. B. U'Ren, C. Silberhorn, K. Banaszek, and I. A. Walmsley, "Efficient conditional preparation of high-fidelity single photon states for fiber-optic quantum networks," Phys. Rev. Lett. **93,** 093601 (2004).

[25] T. Suhara, H. Okabe, and M. Fujimura, "Generation of polarization-entangled photons by type-II quasi-phase-matched waveguide nonlinear-optic device," IEEE Photon. Technol. Lett. **19,** 1093–1095 (2007).

[26] M. Fiorentino, S. M. Spillane, R. G. Beausoleil, T. D. Roberts, P. Battle, and M. W. Munro, "Spontaneous parametric down-conversion in periodically poled KTP waveguides and bulk crystals," Opt. Express **15,** 7479–7488 (2007).

[27] A. Martin, V. Cristofori, P. Aboussouan, H. Herrmann, W. Sohler, D. B. Ostrowsky, O. Alibart, and S. Tanzilli, "Integrated optical source of polarization entangled photons at 1310 nm," Opt. Express **17,** 1033–1041 (2009).

[28] G. Fujii, N. Namekata, M. Motoya, S. Kurimura, and S. Inoue, "Bright narrowband source of photon pairs at optical telecommunication wavelengths using a type-II periodically poled lithium niobate waveguide," Opt. Express **15,** 12769-12776 (2007).

[29] W. Tittel, J. Brendel, H. Zbinden, and N. Gisin, "Quantum cryptography using entangled photons in energy-time Bell states," Phys. Rev. Lett. **84,** 4737-4740 (2000).

[30] T. Honjo, S. W. Nam, H. Takesue, Q. Zhang, H. Kamada, Y. Nishida, O. Tadanaga, M. Asobe, B. Baek, R. Hadfield, S. Miki, M. Fujiwara, M. Sasaki, Z. Wang, K. Inoue, and Y. Yamamoto, "Long-distance entanglement-based quantum key distribution over optical fiber," Opt. Express **16,** 19118–19126 (2008).

[31] H. Takesue, E. Diamanti, C. Langrock, M. M. Fejer, and Y. Yamamoto, "10-GHz clock differential phase shift quantum key distribution experiment," Opt. Express **14,** 9522–9530 (2006).

[32] C. E. Kuklewicz, M. Fiorentino, G. Messin, F. N. C. Wong, and J. H. Shapiro, "High-flux source of polarization-entangled photons from a periodically poled $KTiOPO_4$ parametric down-converter," Phys. Rev. A **69,** 013807 (2004).

[33] C. K. Hong, Z. Y. Ou, and L. Mandel, "Measurement of subpicosecond time intervals between two photons by interference," Phys. Rev. Lett. **59,** 2044–2046 (1987).

[34] K. Sanaka, K. Kawahara, and T. Kuga, "New high-efficiency source of photon pairs for engineering quantum entanglement," Phys. Rev. Lett. **86,** 5620–5623 (2001).

[35] D. A. Kleinman, "Theory of optical parametric noise" Phys. Rev. **174,** 1027–1041 (1968).

[36] K. Koch, E. C. Cheung, G. T. Moore, S. H. Chakmakjian, and J. M. Liu, "Hot spots in parametric fluorescence with a pump beam of finite cross section," IEEE J. Quantum Electron. **31,** 769–781 (1995).

[37] E. C. Cheung, Karl Koch, Gerald T. Moore, and J. M. Liu, "Measurements of second-order nonlinear optical coefficients from the spectral brightness of parametric fluorescence," Opt. Lett. **19,** 168-170 (1994).

[38] Z. Y. Ou and Y. J. Lu, "Cavity enhanced spontaneous parametric down-conversion for the prolongation of correlation time between conjugate photons," Phys. Rev. Lett. **83,** 2556-2559 (1999).

[39] R. L. Byer and S. E. Harris, "Power and bandwidth of spontaneous parametric emission," Phys. Rev. **168,** 1064–1068 (1968).

[40] J. D. Bierlein and H. Vanherzeele, "Potassium titanyl phospate: properties and new applications," J. Opt. Soc. Am. B **6,** 622–633 (1989).

[41] T. E. Murphy, Ph.D. thesis, MIT (2001). See also the package for numerically solving the eigenmode problem at http://www.photonics.umd.edu/software.

[42] K. Kato, "Temperature Insensitive SHG at 0.5321 μm in KTP," IEEE J. Quantum. Electron. **28**, 1974-1976 (1992).

[43] R. G. Batchko, D. R. Weise, T. Plettner, G. D. Miller, M. M. Fejer, and R. L. Byer, "Continuous-wave 532-nm-pumped singly resonant optical parametric oscillator based on periodically poled lithium niobate," Opt. Lett. **23,** 168-170 (1998).

[44] T. Suhara and H. Nishihara, "Theoretical analysis of waveguide second-harmonic generation phase matched with uniform and chirped gratings," IEEE J. Quantum. Electron. **26**, 1265-1276 (1990).

[45] M. M. Fejer, G. A. Magel, D. H. Jundt, and R. L. Byer, "Quasi-phase-matched second harmonic generation: tuning and tolerances," IEEE J. Quantum. Electron. **28**, 2631-2654 (1992).

[46] O. Kuzucu, M. Fiorentino, M. A. Albota, Franco N. C. Wong, and Franz X. Kärtner, "Two-photon coincident-frequency entanglement via extended phase matching," Phys. Rev. Lett. **94,** 083601 (2005).

[47] T. Kim, M. Fiorentino, P. V. Gorelik and F. N. C. Wong, "Low-cost nanosecond electronic coincidence detector," arXiv: physics/0501141 (2005).

[48] P. L. Voss, K. G. Köpfrülü, S.-K. Choi, S. Dugan, and P. Kumar, "14 MHz rate photon counting with room temperature InGaAs/InP avalanche photodiodes," J. Mod. Opt. **51,** 1369–1379 (2004).

[49] G. Ribordy, N. Gisin, O. Guinnard, D. Stuck, M. Wegmuller, and H. Zbinden, "Photon counting at telecom wavelengths with commercial InGaAs/InP avalanche photodiodes: Current performance," J. Mod. Opt. **51,** 1381–1398 (2004).

[50] O. Kuzucu, F. N. C. Wong, S. Kurimura, and S. Tovstonog, "Time-resolved single-photon detection by femtosecond upconversion," Opt. Lett. **33,** 2257–2259 (2008).

[51] J. Chen, A. J. Pearlman, A. Ling, J. Fan, and A. Migdall, "A versatile waveguide source of photon pairs for chip-scale quantum information processing," Opt. Express **17,** 6727–6740 (2009).